Summer Mélange Stabilizes Rifting Terminus Ice at Rink Isbrae, West Greenland

A Thesis
Presented in Partial Fulfillment of the Requirements for the
Degree of Master of Science
with a
Major in Geology
in the
College of Graduate Studies
University of Idaho
by

Emma S. Swaninger

Major Professor: Timothy C. Bartholomaus, Ph.D.
Committee Members: Jerry Fairley, Ph.D.; Vibhav Durgesh, Ph.D.
Department Administrator: Leslie Baker, Ph.D.

August 2020

Authorization to Submit Thesis

This thesis of Emma S. Swaninger, submitted for the degree of Master of Science with a Major in Geology and titled "Summer Mélange Stabilizes Rifting Terminus Ice at Rink Isbrae, West Greenland," has been reviewed in final form. Permission, as indicated by the signatures and dates below, is now granted to submit final copies to the College of Graduate Studies for approval.

Major Professor: _____ Date: _____
Timothy Bartholomaus, Ph.D.

Committee Members: _____ Date: _____
Vibhav Durgesh, Ph.D.

_____ Date: _____
Jerry Fairley, Ph.D.

Department Administrator: _____ Date: _____
Leslie Baker, Ph.D.

Abstract

Ice mélange is a densely packed, granular material consisting of icebergs bound together with sea ice in a rigid matrix at glacier termini. Ice mélange has been shown to affect glacier stability and terminus dynamics at some tidewater glaciers by influencing glacier advance and retreat, inhibiting calving, changing fjord circulation, and altering near surface ocean temperatures which can change iceberg melt rates. Prior studies have focused on extreme cases of mélange formation where mélange exists year-round or in winter. These studies indicate that mélange can provide significant back stress or a “buttressing” effect on the terminus through lateral resistance with fjord walls and dynamic jamming of mélange which creates large localized resistive stresses. For some Greenland glaciers, a short-lived mélange can develop following winter mélange disintegration and this mélange’s ability to impact terminus flow is undetermined. Here, I illustrate the capability of short-term, summer mélange at Rink Isbræ, West Greenland to compress and stabilize a rifting piece of terminus, that we term a loose "ice tooth," torn open following three large calving events ranging in surface area from 0.22 km^2 to 0.64 km^2. Using terrestrial radar interferometry, I analyze variations in glacier and mélange velocities within 0.5 km of the terminus of Rink Isbrae during calving events, evaluate mélange rigidity, and determine the forces acting on a calving iceberg to estimate the shear strength of terminus ice at Rink Isbrae. While the mélange did not affect flow of fully attached glacier ice, mélange indirectly influences glacier dynamics by 1) compressing developing mélange on the ice tooth, which slowed down the ice tooth after calving, and 2) temporarily stabilizing the ice tooth as the mélange developed through ice-to-rock contact along the fjord walls. The in-situ terminus shear strength I find, 50 kPa to 540 kPa, falls on the low end of shear strengths of ice proposed by prior field and theoretical experiments, which have been observed to fall between 200 kPa and 1000 kPa. The shear strength of ice is not well constrained due to lack of observational data, and this measurement may be more representative of a material property at actual tidewater glaciers than measurements developed from models in prior research. Additionally, slab capsize calving creates a domino effect where more calving is triggered through rifting of ice laterally connected to the calving iceberg. In Greenland, other tidewater glaciers that display slab capsize calving and have semi-confined to confined fjords have analogous mélange occurrences which suggests that summer mélange is important when considering short-term calving behavior and long-term glacier evolution.

Acknowledgements

I want to express my appreciation and most sincere gratitude to my major advisor, Dr. Timothy C. Bartholomaus. His constant encouragement, unyielding positive attitude, and tangible compassion for the difficulties of research are completely unmatched by any academic I have encountered. His gentle reminders to not be so hard on myself or my research as well as grounding me when my words were tangled in my head are beyond what I could have hoped for in an advisor. Thank you, Tim, I cannot emote all the ways you have been instrumental to my success and sanity.

I wish to also express thanks to everyone who has contributed the collection of data and completion of this project: Dr. Ginny Catania at University of Texas – Austin and Dr. Leigh Stearns at University of Kansas for their support and expertise in the field and making data acquisition possible. Dr. Mark Fahnestock at University of Alaska – Fairbanks for taking the time to teach the project team the intricacies of the terrestrial radar interferometer and allowing them to use the instrument at Rink Isbrae.

Thank you so much to my committee members Dr. Jerry Fairley and Dr. Vibhav Durgesh for being supportive and being on my committee. Thank you also to Dr. Eric Mittelstaedt for your guidance and delightful attitude.

I would also like to thank the National Aeronautics and Space Administration Cryospheric Sciences program who funded the grant (NNX12AP50G) that made the data collection for this thesis possible.

Additional thanks and love to my community of humans who have quickly become my closest friends, partners, and family. Your constant presence, unwavering and unprecedented support, and nurturing hearts have really changed my life. You've encouraged me to believe in myself, fight for myself, and open myself up to a new, fractal world full of pigment, light, art, and theater.

A special thank you to the cast members of my favorite podcast, Hello from the Magic Tavern. You have given me joy and laughter on days when it was most difficult.

Dedication

I would like to dedicate this work to my perfect and hardworking parents, Debi Patton and Douglas Swaninger, my incredibly supportive, kind step-parents, Charlie Patton and Dawn Swaninger, my unconditionally loving grandparents, Betty and Jake Swaninger, and Barbara and Bill Montgomery, my inspiring thoughtful sister Tabitha Swaninger, and my other half and best friend of 20 years, Emily Beasley. If I have learned anything, it has been that I know nothing, and that the best parts of my life are and have ALWAYS been family. You are the only rocks that I know stay steady.

Table of Contents

List of Figures

List of Tables

1. Introduction

In the last two and a half decades tidewater glaciers worldwide have experienced rapid changes controlled by processes occurring at glacier termini (Rignot and Kanagaratnam, 2006; Nick and others, 2009). In that time, a rapidly warming climate and the acceleration and retreat of many tidewater glaciers have contributed to mass loss at the world's ice sheets (Rignot and Kanagaratnam, 2006; van den Broeke and others, 2009; Rignot and others, 2011; Hanna and others, 2012; Enderlin and others, 2014). Tidewater glaciers have been postulated to change due to increases in surface melt water runoff (Smith and others, 2017), sublimation (Box and Steffen, 2001), submarine melting (Bartholomaus and others, 2013; Enderlin and others, 2013; Fried and others, 2015), and iceberg calving (Enderlin and others, 2014; Andersen and others, 2015). Ice loss caused by these processes have led to a negative surface mass balance on the Greenland Ice Sheet and has made Greenland one of the largest contributors to sea level rise (Andersen and others, 2015; Khan and others, 2015). Of the mechanisms leading to mass loss and frontal retreat at tidewater glaciers, iceberg calving continues to be one of the most challenging parameters to model and predict (O'Leary and Christoffersen, 2013; Benn and others, 2017; Amaral and others, 2020).

Iceberg calving is one of the most important processes contributing to ice sheet mass loss, changes in tidewater glacier evolution, and sea level rise (Benn and others, 2007; Holland and others, 2016). Alongside submarine melt, calving makes up around one third to one half of ice lost from the Greenland Ice Sheet (Enderlin and others, 2014; Rignot and Kanagaratnam, 2006). Calving is an episodic process that occurs when tensile, compressive, and shear stresses within a glacier reach a critical failure point that lead to the formation and propagation of surface and basal fractures, and eventual ice detachment (Bassis and Walker, 2012; Bassis and Jacobs, 2013). The stability and failure of calving icebergs continues to be difficult to understand due to the diversity in calving behavior in various glacial systems and lack of empirical observation of calving events (Bassis and Walker, 2012). Diversity in calving has given rise to multiple calving criteria that attempt to model, constrain, and predict calving behaviors that can vary across time and glacial regions (Benn and others, 2007; Amaral and others, 2020). While there has been incredible advancement in calving research, current models do not sufficiently describe the complexities of calving processes (Benn and others, 2017).

Observations at tidewater glaciers have shown a strong connection between calving and glacier flow (Howat and others, 2005). Calving affects glacier flow by decreasing basal and lateral resistance at the terminus which causes acceleration of up-glacier ice and contributes to glacier thinning and retreat (Joughin and others, 2012; Nick and others; 2012; Bondzio and others, 2016). Calving is modulated by glacier ice thickness, fjord bathymetry, and ice-ocean interactions like submarine melt, sea ice presence, and ice mélange development (Amundson and others, 2010; Medryzcka and others, 2016; Robel, 2017). An irregular relationship exists between the presence of ice mélange and calving, and recent studies propose

that ice mélange may affect the stability of tidewater glaciers by modifying glacier geometry and glacier flow (Joughin and others, 2012; Peters and others, 2015).

Ice mélange, hereafter called mélange, in glaciology is a coarse, granular body of icebergs and sea ice that rests on the ocean's surface, is rigidly trapped in front of a tidewater glacier, and is temporarily bound to the fjord walls and the glacier terminus (Amundson and others, 2010; Howat and others, 2010; Walter and others, 2012). Depending on salinity, sea temperature variability, and ice temperature, energy exchange between warmer fjord water and colder calved icebergs can decrease water temperatures enough to freeze the ocean surface to form sea ice, trap icebergs, and develop mélange (Howat and others, 2010; Walter and others, 2012; Peters and others, 2015), even when air temperatures are insufficient to freeze the sea surface on their own. Processes affecting mélange development, geometry, and longevity vary in different fjords, but are dependent on iceberg productivity, horizonal wind forcing, fjord constriction, changes in ocean circulation and temperature, atmospheric variability, fjord geometry, glacier acceleration, and retreat of the calving front (Howat and others, 2010; Vieli and Nick, 2011; Walter and others, 2012; Foga and others, 2014; Peters and others, 2015; Amundson and Burton, 2018; Burton and others, 2018).

In winter months the decreasing air and ocean temperatures around Greenland facilitate sea ice growth to form winter mélange that grows outward from the terminus and reaches its maximum areal coverage in April or early May (Howat and others, 2010). In early spring, when atmospheric temperatures start to increase and the mélange starts to disintegrate, calving rates locally increase at tidewater glaciers in both Greenland and Antarctica (Scambos and others, 2009; Howat and others, 2010; Amundson and others, 2010). Winter mélange is suggested to be more rigid and slow moving due to wintertime sea ice thickening, while mélange remaining after the initial spring collapse is more mobile and free floating around the fjord (Sundal and others, 2013; Foga and others, 2014; Peters and others, 2015). Lingering mélange matrices that have not yet circulated away from the fjord during the spring disintegration tend to have higher percentages of icebergs to sea ice due to the increased iceberg production through calving (Amundson and others, 2010). Additionally, iceberg motion in mélange matrices are driven by horizontal, along-fjord winds and ocean currents (Sutherland and others, 2014). Some glaciers, like Jakobshavn Isbrae, Helheim Glacier, and Kangerdlugssauq Glacier, have persistent mélange all year long while other glaciers develop seasonal, temporary mélange in the winter that collapses in the spring (Howat and others, 2005; Joughin and others, 2012; Moon and others, 2015; Peters and others, 2015; Amundson and Burton, 2018). Occasionally, in summer and fall months at some tidewater glaciers, a transitory mélange occurs that can persist for mere days or weeks before disintegrating and leaving the glacier front (Amundson and others, 2020). The seasonal strength or rigidity of mélange mechanically influences glacier flow and can modify calving behavior (Walter and others, 2012), but has not been quantified for occurrences of transitory, summer mélange.

Recent research has suggested that seasonal mélange can influence glacier dynamics. When ocean currents and prevailing surface winds fail to expel the mélange from the fjord, the mélange is able to alter fjord circulation by hindering ocean-to-terminus interactions (Amundson and others, 2010; Sutherland and others, 2014), provide a buttressing effect or back-stress on the glacier terminus that can inhibit calving (Howat and others, 2010; Amundson and others, 2012; Walter and others, 2012; Cassotto and others, 2015), and secondarily affect glacier flow (Podrasky and others, 2014; Peters and others, 2015; Robel, 2017; Burton and others, 2018). Several recent summer and winter studies in Greenland have endeavored to observe, model, and quantify the complexities of mélange's relationship with the calving front of glaciers using time-lapse imagery (Medryzcka and others, 2016; Cassotto and others, 2015; Peters and others, 2015), synthetic aperture radar (Cassotto and others, 2019; Peters and others, 2015; Xie and others, 2016; Burton and others, 2018, Amundson and others, 2020), global positioning system (GPS) (Amundson and others, 2010; Sutherland and others, 2014), satellite imagery (Howat and others, 2010; Foga and others, 2014; Moon and others, 2015; Cassotto and others, 2015, Fried and others, 2018), and discrete-element modeling (Robel, 2017; Burton and others, 2018). Theoretical and observational data from these studies suggest that through ice-to-ice and ice-to-fjord wall contact at the shear margins, mélange can affect a glacier terminus position, near terminus speeds, calving style, and seasonal calving rate (Peters and others, 2015; Robel, 2017). Locally, modeled shear stresses in seasonal mélange can be large enough to suppress kilometer sized icebergs from calving (Burton and others, 2018). Even so, mélange's ability to influence terminus behavior is time dependent and varies among glacier fjords (Moon and others, 2015; Fried and others, 2018).

Slab capsize calving events, also called full-glacier thickness calving, dominate glacier mass loss at tidewater glaciers (Amundson and others, 2010). Slab capsize calving occurs when a glacier advances into deeper water, becomes ungrounded, the terminus ice thins, approaches floatation, and super-buoyant conditions begin to force the ungrounded ice upward (Medrzycka and others, 2016; Sergeant and others, 2019). Super-buoyant conditions arise when the terminus of the glacier is forced below buoyant equilibrium and is subjected to upward buoyant forces (Benn and Åström, 2018). These buoyant forces can lead to the propagation of basal fractures, as a result of flexural stresses, and eventual calving (Sergeant and others, 2019). Fractures found at the surface and base of glaciers, called crevasses, are indicators of deformation and stress within the glacier ice (Colgan and others, 2016). Basal crevasses experience high tensile stresses and are expressed on the surface of the glacier as locally depressed regions (James and others, 2014; Murray and others, 2015). Slab capsize calving events at or near these depressed regions can last several days due to the rate of basal crevasse propagation and speed of rotation of the icebergs before failure (Xie and others, 2016; Sergeant and others, 2018). Propagation of crevasses and buoyancy forces leading to calving is dependent on the states of stress within the glacier (Bassis and Walker, 2012).

States of tensile, compressive, and shear stress are created by ice overburden and pressure gradients within the glacier and are influenced by ice flow, buoyancy forces, melt undercutting, buttressing capabilities of ice mélange, and hydrostatic force imbalance (Van der Veen, 1996; Ma and Bassis, 2019; Amaral and others, 2020). On small, laboratory scales, the strength and mechanical behavior of ice has been shown to be non-linear and difficult to constrain due to a host of ice characteristics that change the internal stress regimes, i.e. ice temperature, salinity, size and distribution of pre-existing fractures, grain-size, and ice strain rates (Fish and Zaretsky, 1997, Schulson and Duval, 2009). While laboratory and theoretically-based research has examined ice failure on micro-to-macro scales, i.e. atomic dislocations, single ice crystal failure, ice core strain, crack initiation and propagation, etc. (Petrenko and Whitworth, 1999; Schulson and Duval, 2009), there is still little work demonstrating the shear strength of in-situ glacier ice, at glacier termini where it governs iceberg calving (Nye, 1957; Frederking and others, 1988; Schulson 1999; Bassis and Walker, 2012). Having a quantitative measurement of shear strength of glacier ice at an actual glacier is essential for improving calculations of tidewater glaciers' overall contribution to mass loss in current numerical ice sheet models.

Despite significant progress, outstanding questions persist concerning 1) the role that ephemeral, summer mélange plays in modulating calving behavior and glacier flow, 2) in-situ shear strengths of glacier terminus ice from actual glacier observations, and 3) terminus responses to slab capsize style calving. High temporal- and spatial-resolution data recording the appearance of daily to week-long, transitory mélange occurrences are required to determine how summer mélange may affect short- and long-term glacier evolution across the Greenland Ice Sheet. Summer mélange may alter the timing and location of calving events, alter fjord water properties and circulation (Enderlin and others, 2016), and modify fjord heat transport (Truffer and Motyka, 2016). Determining the shear strength of terminus ice during calving in a real glacial setting is a direct experimental representation of a material property that is necessary for defining stress conditions necessary for predicting where failure occurs in glacier ice (Petrenko and Whitworth, 1999; Schulson and Duval, 2009). Therefore, quantifying interactions between glacier motion, fracture behavior, calving activity, and mélange presence will allow better characterization of complex calving processes, more accurate stress parameterizations in ice sheet modeling, and help predict terminus evolution in diverse glacial regions.

To meet these needs, I use an 8-day long record of terrestrial radar interferometry observations of brief, summer mélange development following three large slab capsize calving events at Rink Isbrae, West Greenland. Prior studies have shown that terrestrial radar interferometry is an effective geophysical surface studies tool that has the capability of monitoring small, rapid surficial changes such as the motion and evolution of mélange and iceberg calving with both high resolution and precision (Werner and others, 2008; Dixon and others; 2012; Caduff and others, 2015; Voytenko and others (a,b), 2015; Xie and others, 2016;

Cassotto and others, 2019). Terrestrial radar interferometry shows detailed observations of the calving front of a glacier by generating high-resolution phase, distance, and radar intensity data in frequent, set intervals on the order of several minutes or less.

The terrestrial radar interferometer is a relatively new and valuable tool, and its unwrapped interferograms are used to evaluate calving behavior, observe mélange motion, and measure velocity changes at the terminus and within the mélange. The radar's intensity images are used to determine rigidity of mélange on the terminus and dimensions of the calving iceberg which are used to estimate the shear strength of ice at the terminus during calving. In this study, mélange forms in a previously ice-free fjord and lasts about a day and a half before breaking apart and circulating away from the terminus. With these data, this study serves to answer the following questions, 1) Is summer mélange strong enough to impact calving, glacier flow, or terminus behavior, if so, how?, and 2) What is the shear strength of ice at the terminus during slab capsize calving at Rink Isbrae?

2. Research Site

Rink Isbræ (71°45′N, 51°40′W) (Fig. 2.1) is a tidewater glacier flowing into Karrat fjord at the northern end of Uummanaq fjord in Qaasuitsup, West Greenland. Rink Isbrae is the seventh largest discharger of ice in Greenland (Enderlin and others, 2014; Fried and others, 2018) and drains an estimated 3.5% of the Greenland Ice Sheet **(**Rignot and Kanagaratnam, 2006). Rink Isbrae's terminus is around 4.5 to 5.5 km wide, has a confined fjord extending ~50 km into Uummannaq Bay, and has a drainage basin around 300,000 km^2 (Rignot and Kanagaratnam, 2006; Medrzycka and others, 2016). Rink Isbrae advances and retreats an average of ±0.5 km annually (Schild and Hamilton, 2013), and over the last 20 years the terminus position has not undergone significant interannual retreat or advance in the way that some large outlet glaciers in Greenland have (i.e. Jakobshavn Isbrae, Petermann Glacier, Helheim Glacier, etc.) (Howat and others, 2010; Box and Decker, 2011; Moon and others, 2014; Medryzcka and others, 2016). Swath-bathymetric data and acoustic-stratigraphic records of bed topography shows central portions of Rink Isbræ's fjord extending 800 to 900 m below sea level and 1000 m further out in the fjord which allows for the terminus to eventually become ungrounded (Dowdeswell and others, 2014; Rignot and others, 2015). Once the terminus becomes ungrounded and advances into deeper water, the central portion of the terminus becomes buoyant and flexes upward which leads to full-thickness slab capsize style calving at Rink Isbrae (Benn and others, 2007; Medryzycka and others, 2016).

Since the early 1990s ice sheet runoff has doubled across Greenland, but at some glaciers in the Uummannaq fjord district, like Rink Isbrae, runoff has increased by only 50% (Rignot and others, 2015). While Rink Isbrae is considered stable, meaning the glacier does not undergo multi-year retreat, the glacier had a negative surface mass balance between 2000 and 2005 (Rignot and Kanagaratnam, 2006). Rink Isbrae's consistent terminus position and lack of retreat is postulated to be caused by subglacial melt rates being significantly lower than the frontal velocity of Rink Isbrae (Rignot and others, 2015; Rignot and others, 2016). Meaning, that for terminus retreat to occur the melt rate must at regularly exceed the frontal velocity of the glacier (Rignot and others, 2015). Instead, calving is the dominate ablation process at Rink Isbrae and melt rates are not able to drive further retreat of the terminus (Rignot and others, 2016). Comparatively, at other glaciers in the Uummannaq fjord district, like Kangilernata Sermia, which is 10 glaciers south of Rink Isbrae, frontal velocity is projected to be lower than estimated melt rates and the terminus has experienced continuous yearly retreat (Rignot and others, 2015). Rink Isbrae is used to study calving behavior and mélange due to its quasi-stable terminus position, ability to develop summer mélange in a clear fjord, and slab capsize style calving.

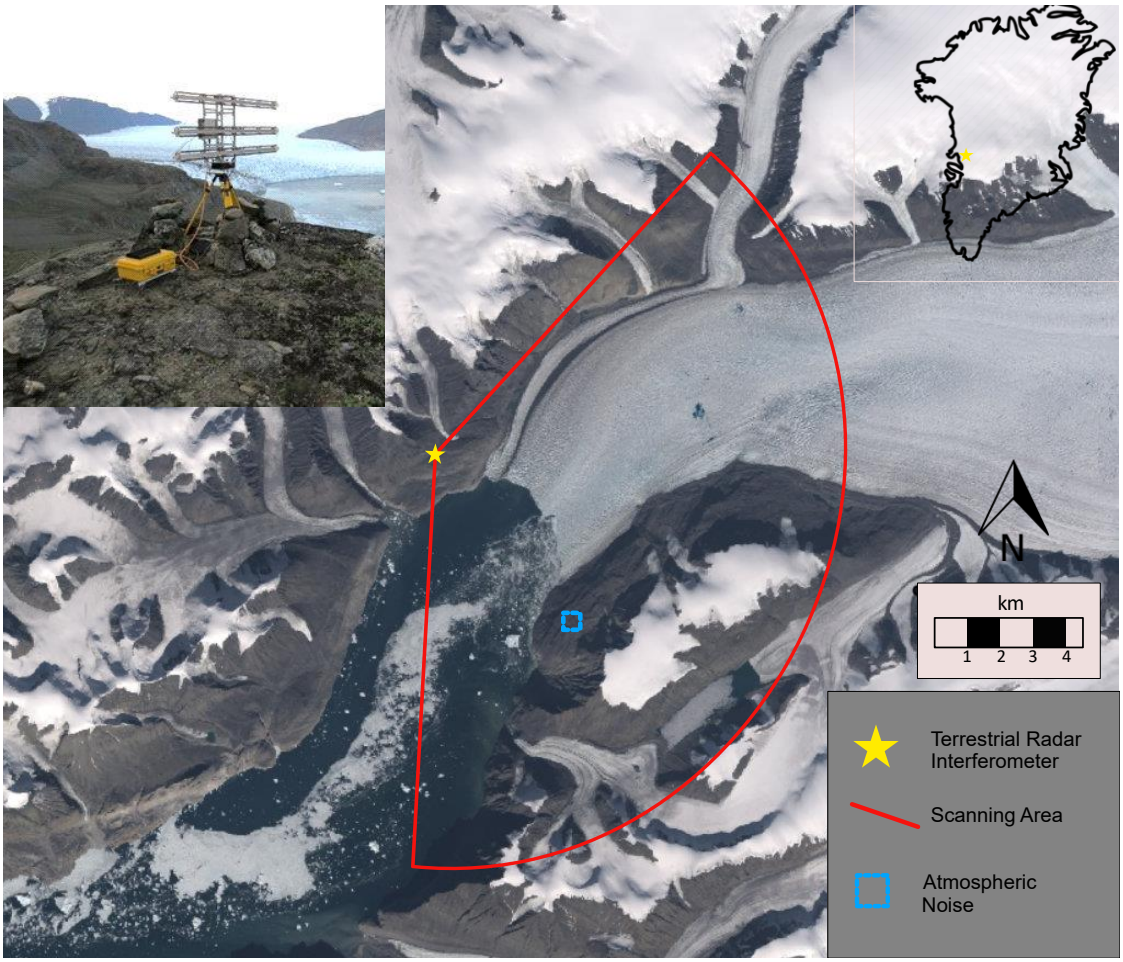

Figure 2.1. Location map (inset) of Rink Isbrae, West Greenland superimposed on Google Earth Engine image of Rink Isbræ from 2 August, 2014, at the end of the campaign. The yellow star indicates the location of the terrestrial radar interferometer. The light blue box at the southern fjord wall is the selected area to describe local atmospheric noise near the glacier. The bulk atmospheric noise area in unwrapped interferograms as described in Section 3.4. In the upper left corner is an image of the terrestrial radar interferometer.

3. Methods

3.1 Terrestrial Radar Interferometry

The terrestrial radar interferometer is a GAMMA portable radar interferometer (GPRI-II), real-aperture radar that is sensitive to line-of-sight displacements on the order of ~1 mm and operates on a Ku-band wavelength (~1.75 cm). The radar has three antennas, one transmitting and two receiving, which allows for repeat topographic mapping during our observation period. The instrument collected measurements with a 155 degree scan reaching a distance ~16 km away for 8 continuous days between July 25th and August 2nd, sampled every 2.5 minutes, and took ~30 seconds to complete each scan. The instrument was positioned above Rink Isbrae, West Greenland (427 m a.s.l) ~3 km away from the terminus on stable bedrock along the northern fjord wall (Fig. 2.1). Each scan was used to generate interferograms, derive line-of-sight velocity maps, and monitor radar image intensity. This radar data is used to analyze glacier and mélange velocities, estimate the shear strength of the terminus ice, track motion of the mélange, and extract iceberg geometries.

To collect data, the radar first scans an area by emitting a microwave beam with a phase coherent signal that reflects off a given surface and returns to the instrument's receiving antenna. Each radar scan contains information about the reflected recorded phase and magnitude of imaged features. Radar scans are then converted into single-look complex images, which contain both amplitude and phase signal information. The amplitude data are used to determine the magnitude of a scan and the phase signal data are used to create interferograms. The single-look complex images are compared to the subsequent image to determine the phase differences between the two scans (Cassotto and others, 2015). If two radar images, when subtracted, are precisely the same regarding surface geometry, antenna polarization, and without atmospheric changes or instrument noise, then the phase difference should be zero everywhere. However, if the images are dissimilar, any non-zero region shows the phase change proportional to the line-of-sight phase difference, which describes motion or displacement in the apparent radar-look direction connecting the radar and a given surface. (Zebker and Lu, 1998). The phase differences are sums of the topographic, atmospheric, displacement, and noise contribution (Caduff and others, 2015). The phase differences are in cycles ranging from 0 to n2π and are projected in differential interferograms, which are colored in the interference color spectrum in the range of a 2π wavelength (Caduff and others, 2015).

To obtain quantitative values for the displacement phase, the differential interferograms are unwrapped to determine the absolute phase. The unwrapping process recognizes phase discontinuities larger than the 2π parameter in the differential interferograms by adding or subtracting appropriate multiples of the 2π parameter to restore the continuity of the phase map (Goldstein and Werner, 1998). The once the interferograms are unwrapped, they can then be converted into line-of-sight displacements and velocities.

The radar's magnitude data are used to create multi-look intensity images or radar intensity images, which are the coherent sum of the radar backscatter data. Radar intensity images do not contain phase data. A multi-look intensity image is the magnitude of the radar signal and describes a target's surface roughness and geometry. Multi-look intensity images spatially appear as illuminated and shadowed topography (Caduff and others, 2015), and are used to feature track glacier and mélange motion, measure the terminus geometry and iceberg lengths, and determine the rotation angle of the calving iceberg.

3.2 Correcting Interferogram Velocities

During 2014, our project team produced 4000 radar interferograms collected between July 25th and August 2nd. From these data, I draw on 681 adaptive filtered unwrapped interferograms from July 28th and 29th to illustrate the glacier response to calving events and 3000 medium-filtered unwrapped interferograms from July 28th and 31st to monitor mélange rigidity and mélange influence on the terminus. Once the interferograms were unwrapped, they were converted to line-of-sight velocities (v_{los}) as given by (Voytenko and others (a,b), 2015):

$$v_{los} = \frac{-\lambda\varphi}{4\pi\Delta t} \qquad (1)$$

$$v_{los} = \frac{-\lambda\varphi}{4\pi * \left(2.5\ min * \frac{1\ day}{1440\ min}\right)} \qquad (2)$$

where λ is wavelength of the radar (λ = 1.75 cm), φ is the unwrapped phase difference, and Δt is the time passed between images. The interferograms were then converted into Cartesian coordinates with 20 m pixel spacing and georeferenced and transferred to UTM coordinates.

If the object that the radar is scanning is not flowing directly at the radar, e.g. the glacier, the line-of-sight velocities need to be corrected to the true flow direction. I correct the line-of-sight velocities to the glacier's true flow velocities using the radar look angle with respect to north ξ, angle of ice motion at the terminus μ, and the line-of-sight velocities in the interferogram (Fig. 3.1). Ice motion direction was found using openPIV, a Python based velocimetry software tool (Taylor and others, 2010), where I used two multi-look intensity images one day apart to cross-reference a 550 x 550 m window with a 450 x 450 m overlap to find correlations in the images to monitor displacements and plot them as flow vectors. Flow direction near the glacier terminus were generally 202° clockwise from north. The angle between line-of-sight velocity and true flow direction velocity at each pixel is found by 360° – μ – ξ to get ω. Flow velocities are then calculated using:

$$v_{gla} = \frac{v_{los}}{\cos\omega} \qquad (3)$$

where v_{gla} is the true glacier velocity and ω is the angle between the line-of-sight velocity and the true glacier velocity.

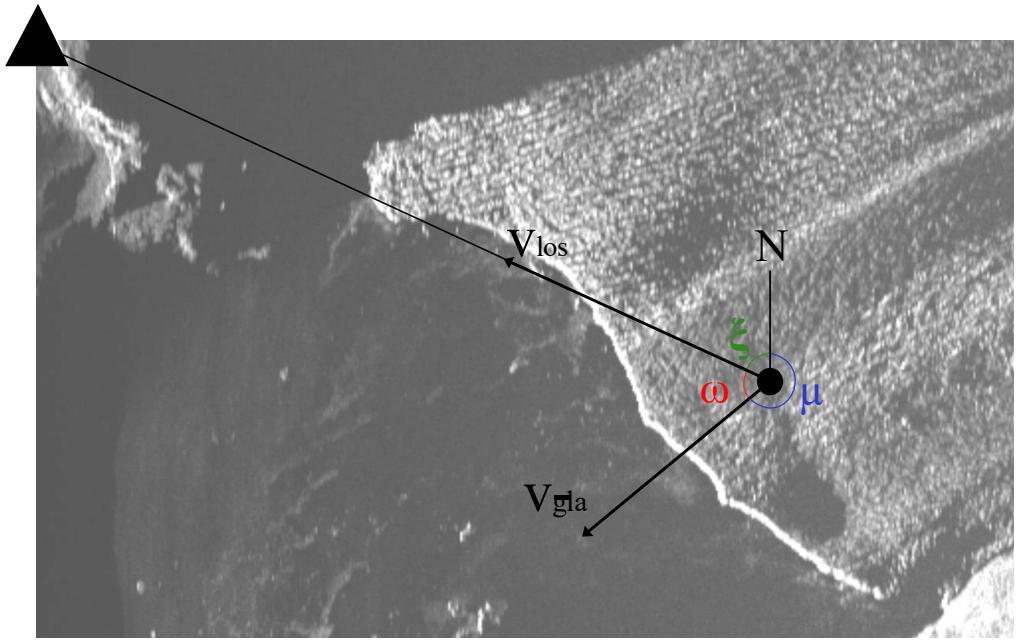

Figure 3.1. Map view diagram of how true glacier velocities (v_{gla}) were calculated and superimposed on opaque multi-look intensity image. The black triangle represents the terrestrial radar interferometer on the fjord wall facing the glacier. The black dot below north represents any position on the glacier with a line-of-sight velocity (v_{los}) to be corrected to true glacier velocity.

3.3 Multi-look Intensity Images

The high spatial resolution of the radar's multi-look intensity images provide insight into the size and magnitude of the calving events and mélange. The multi-look intensity images provide independent measurements that can be employed to measure surface displacement, track surface geometries and distances, and assess glacier and mélange motion. The multi-look intensity images are used track mélange and glacier flow direction with openPIV and measure iceberg geometry to estimate the contact force and shear strength of the terminus ice during calving as explained in Section 5.2.1 and 5.2.2.

3.4 Atmospheric Corrections

Atmospheric noise variations can impact the radar acquisitions by changing the index of refraction and thereby influencing the electromagnetic wave velocity and measured phase (Cassotto and others, 2015). Noise within the interferograms may be caused by atmospheric temperature, air pressure, humidity, and unwarranted phase shifts (Goldstein and Werner, 1998; Caduff and others, 2015). Even on during short observation times on the order of minutes, atmosphere can contribute to localized perturbations in the

interferograms (Caduff and others, 2015). To minimize noise during the unwrapping process the interferograms were smoothed with an adaptive filtering algorithm that improves the signal-to-noise ratio of fringes in differential interferograms (Goldstein and Werner, 1998; Cassotto and others, 2015). The adaptive filtering algorithm performs a Fourier spectrum of a set window size and uses pixel groups with good coherence to weight the filtered data, while areas of low coherence are excluded (Goldstein and Werner, 1998). Fringes are a result of the differences in interference between the beams of two radar images. Regions with high fringe rates indicate areas of high deformation.

Even with a filter to minimize atmospheric noise, random noise still affects the unwrapped interferograms. To account for bulk atmosphere near the glacier, the velocities of a 400 x 400 m area on the far fjord wall nearest to the terminus were used to monitor heterogeneity in the atmosphere at each scan (Fig. 2.1 – light blue square). We expect that the fjord wall should be immobile and any non-zero velocity can be attributed to atmospheric noise. The fjord wall velocities are used to represent the atmospheric noise because it is closest to the terminus and should be most comparable to atmosphere that may be influencing nearby glacier speeds. As explained in the following, noise found at the fjord wall be partially removed from the glacier velocities to eliminate one noise source within the interferograms.

To find the amount of noise present, for each interferogram, I determine the median of the 400 velocities drawn from the fjord wall. I then subtract the median fjord wall velocity, or average amount of atmospheric noise, that corresponds with a velocity taken on the glacier. The median velocities from the fjord wall vary from 0 to ±2 m d^{-1} (Fig. 3.2 – A). I take the interquartile range of the fjord wall velocities which describe the spread of values between the 25^{th} and 75^{th} percentile of a given sample to see how spread out atmospheric noise is along the fjord wall. The interquartile range for the fjord wall velocities are distanced by a maximum of 1 m d^{-1} (Fig. 3.2 – B). Since there is still random noise causing erratic spikes in the raw glacier velocities (Fig. 3.2 – C). To get a clearer view of glacier motion, I take the raw glacier velocities, with the median removed, and plot a one-hour averaged running average velocity time series of the glacier (Fig. 3.2 – C). To do this, I use a moving window or convolution approach which takes a fixed number of velocities, sums those velocities together, and divides them by the total number of input velocities. Setting the window in hour intervals, an average velocity at each time interval is obtained by dropping the value at the end of the sequence and adding the next point to calculate a new average. In later evaluations of glacier and mélange velocities, I will also be employing similar running averages to the glacier and mélange velocities.

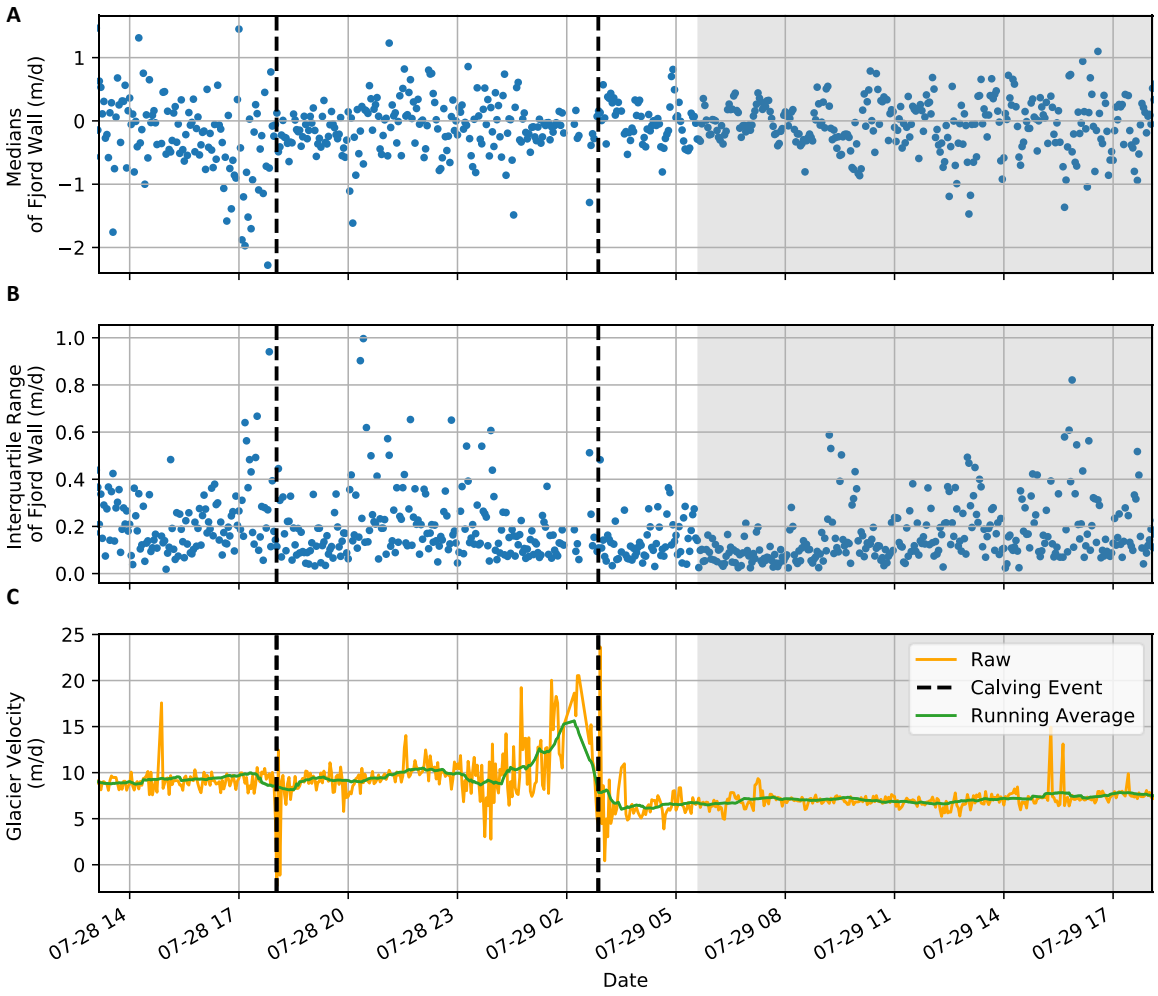

Figure 3.2. Interferometric atmospheric noise correction workflow. A) Atmospheric noise medians drawn from fjord wall data. B) Atmospheric noise interquartile ranges from fjord wall data. C) Raw glacier velocities (orange) with fjord medians removed. One-hour running average of glacier velocities (green) used to approximate average glacier motion similar to Figure 4.1 – C.

4. Results

4.1 Record

4.1.1 *Calving*

Over the complete deployment of the terrestrial radar interferometer, there were two large and one smaller slab capsize calving events. These calving events, easily observed in multi-look intensity images and the interferograms, had surface areas of approximately 0.82 km^2, 0.74 km^2, and 0.32 km^2. The larger calving events were observed by the radar on July 26th sometime between 01:32:30 and 10:40:00 UTC, July 28th at 18:02:00 UTC, and July 29th at 02:52:00 UTC. The first event, while not directly captured with interferometry data due to radar error, was visible in the retreat of the calving front. The first and second calving events were almost the full width of the terminus, ~3.3 km and ~3.0 km, while the third calving event was smaller and centrally positioned on the glacier, ~1.3 km in length (Fig. 4.1 – B).

Prior to any recorded calving events, surface rifts and a depressed region of terminus where calving events would occur were already detectable in multi-look intensity images. Once the resistive support from the ice calved during the second event was removed, a 2.3 km wide portion of terminus ice, indicated in multi-look intensity images by a large rift and depressed, shadowed region on the terminus began to rotate outward as it prepared to calve (Fig. 4.1 – B). The southern portion of the iceberg near the shadowed area began rotating and accelerating faster than the northern portion of iceberg that was more connected to thinner, grounded terminus ice. The force from the rotation of the southern portion of iceberg, which was kept from calving by its attachment to the northern iceberg, caused the northern portion to start rifting and pulling away from the terminus. During rotation, a fracture formed between the northern portion of iceberg, hereafter called ice tooth, and southern portion of the iceberg at 23:27:00 UTC on 28 July. This fracture was seen in differential interferograms as discontinuous phase fringes and in the adaptive-filtered interferograms as a discontinuity in the unwrapped velocities in the glacier.

To monitor Rink Isbrae's change in velocity, I use unwrapped interferograms to investigate one-hour running average of glacier and ice tooth velocities between 13:00:00 UTC on 28 July and 18:10:00 UTC on 29 July (Fig. 4.1 – C). Once the fracture between the ice tooth and iceberg developed, the iceberg accelerated from 10 to 20 m d^{-1} and the ice tooth accelerated from 10 m d^{-1} to 15 m d^{-1} over the next three hours. One hour before the third calving event at 01:42:00 UTC on 29 July the iceberg and ice tooth reached peak velocity and then rapidly decreased. However, in the differential interferograms there was a high fringe rate indicating high deformation or movement in that area. Therefore, during signal processing, the fringe rate was probably being aliased by the unwrapping algorithm, which caused cycles to be skipped and signals become distorted, because we would expect the velocities to continue to increase until calving. Meanwhile, up-glacier, fully attached ice that was not obviously rifting away from the glacier accelerated an average of 1.5 to 3 m d^{-1} until the third calving event and resumed its average velocity afterward.

4.1.2 *Mélange*

During this campaign, the fjord was open and completely free of any mélange until the second and third calving events. The first calving event's iceberg disintegrated into the waters without generating any mélange and smaller icebergs and debris circulated out of the fjord early on 27 July. The second calving event's iceberg broke apart and dispersed into the fjord reaching 5 km from the calving front and developed small amounts of mélange near the terminus reaching ~0.7 km outward around 22:30:00 UTC on 28 July. The third calving event disrupted mélange development but added more icebergs to the fjord, and mélange began to reharden near the terminus around 09:30:00 UTC on 29 July to develop a more extensive, rigid mélange.

4.2 Mélange Rigidity

4.2.1 *Unwrapped Line-of-Sight Velocities*

The rigidity of the mélange was quantified by first evaluating motion close and far away from the terminus in a half-hour median-filtered running average line-of-sight velocity time series (Fig. 4.2 – A). Following the third calving event, line-of-sight mélange velocities began to converge to a constant value first at the terminus and then further out in the fjord. Mélange was deemed hardened in the interferograms as smooth, continuous surfaces in the fjord; visually similar to the glacier surface in Figure 4.2 – A. While the mélange remained in the fjord, unwrapped interferograms show repeated sequences of refreezing and re-fracturing within the matrix seen as fractures within the smoothed surface of the mélange once the mélange is rigid. The mélange stayed relatively rigid until around 20:00:00 on 30 July (Fig. 4.2 – A), when the mélange began to speed up become more mobile in the fjord. At 23:50:00 UTC on 30 July, a small serac style calving event on the southern portion of the glacier terminus causes the rest of the mélange to loosen, start to disintegrate, and fully circulate away from the terminus by the 31 July.

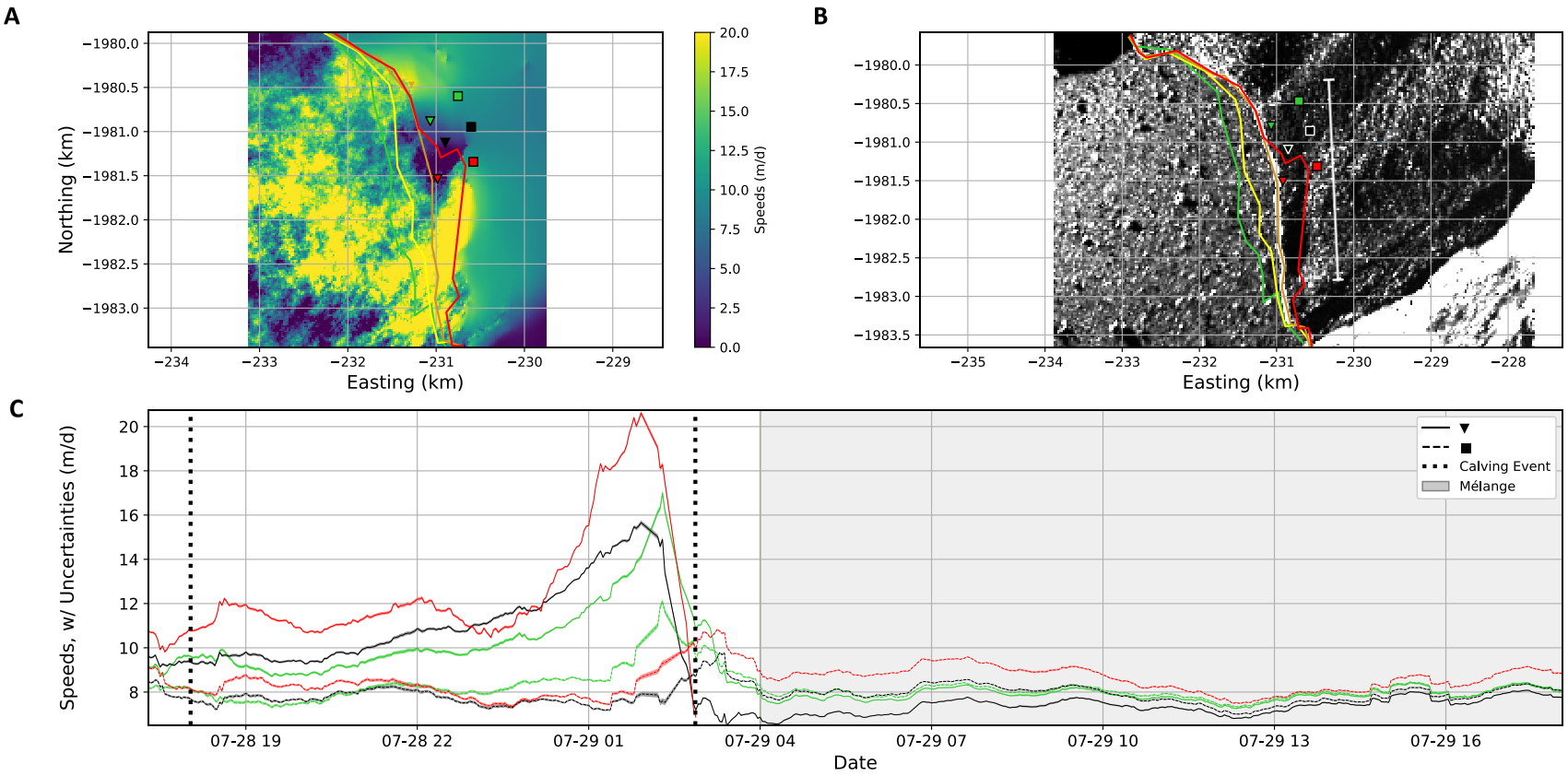

Figure 4.1. A) Georeferenced adaptive filtered interferogram with terminus velocity positions that coordinate with the one-hour running average velocity time series in (C). B) Multi-look intensity image from 23:02:30 UTC on 28 July that is geo-rectified and rotated showing the depression shadow caused by iceberg flexure, the length of surface rift ~2.3 km (white line) where ice tooth and calving iceberg connect, and the terminus profile lines at the start of the campaign (green) and after the first (yellow), second (orange), and third (red) calving event. The six velocity positions are also placed on this image for reference. C) One- hour running average velocity time series for ice tooth and glacier ice. Dotted lines indicate glacier ice and solid lines indicate ice on the ice tooth or in the mélange.

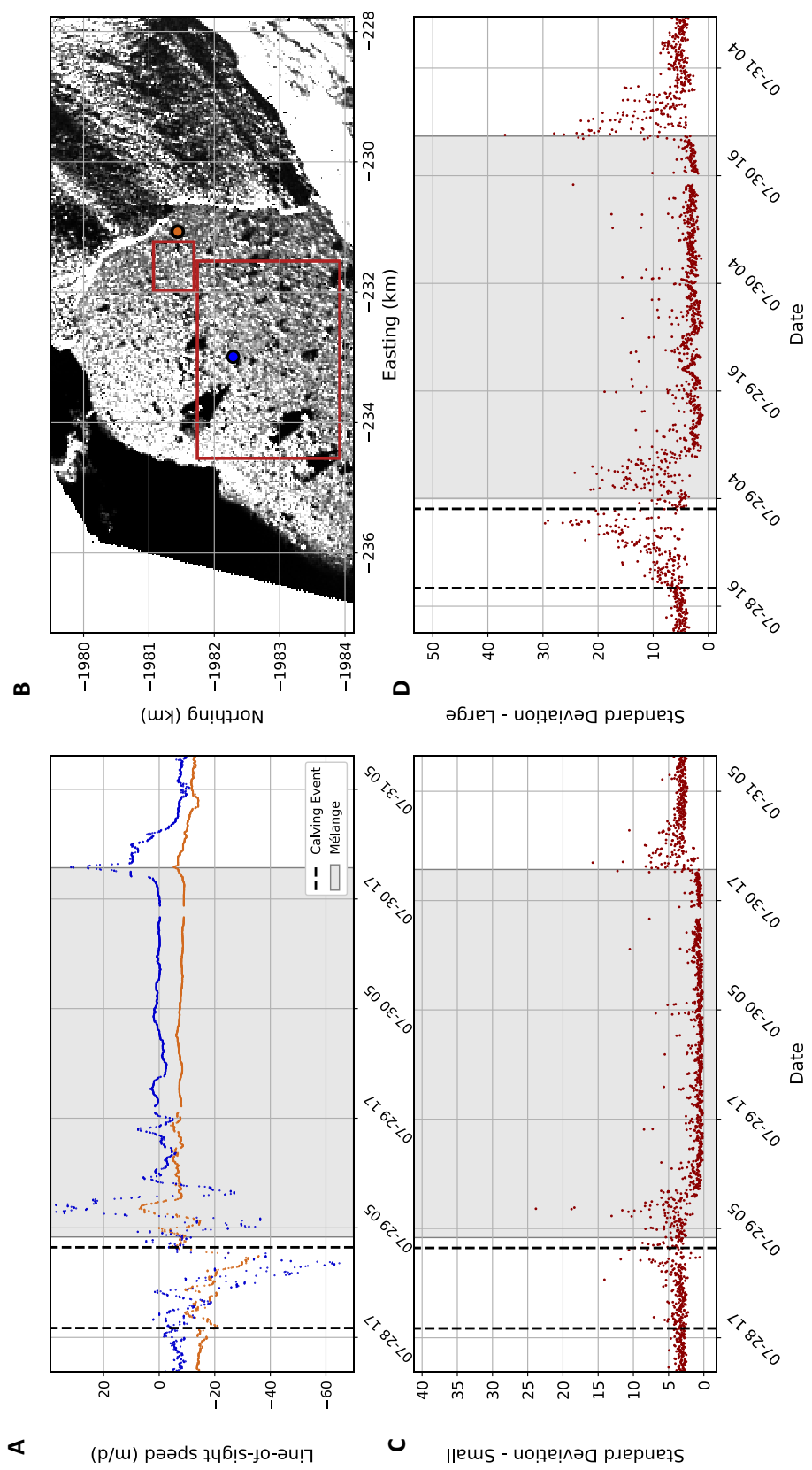

Figure 4.2. A) Line-of-sight half-hour averaged velocity time series close to the terminus (gold) and in the center of the fjord (blue). B) Georeferenced and rotated multi-look intensity image with mélange positions (gold and blue – dots). A negative speed, in this case, means that the pixel is moving away from the radar. C) Standard deviation of unsmoothed velocity values in small rectangle near the terminus. D) Standard deviation of unsmoothed velocity values in large rectangle in central area of mélange.

4.2.2 *Standard Deviation of Motion within Mélange*

To determine the endurance of mélange rigidity across the dataset, I sample a small and large rectangular area within the mélange to find the standard deviation of the line-of-sight velocities within the mélange matrix (Fig. 4.2 – B). The standard deviation represents the variation within a sample of mélange velocity values that serves as a proxy for the population value. The section closest to the terminus serves to show rigidity near the calving front, and the larger section serves to describe rigidity of the larger, central area of mélange. A large standard deviation indicates values with a wider spread about the mean of distribution, and inversely, small standard deviation indicate a narrower spread. Within the standard deviation time series, areas that have similar velocities or are semi-rigid to rigid have small standard deviations.

At the terminus, where mélange first starts forming there is a brief settling period, between 04:00:00 and 05:30:00 UTC on the 29 July, where the standard deviation values vary between 2 to 5 m d^{-1}. Several serac calving events between 05:45:00 and 06:20:00 UTC on the 29 July increased the velocity variability in the mélange. Standard deviations in both portions begin to approach zero or become stabilized around 08:30:00 to 09:00:00 UTC on the 29 July. Mélange was continuously rigid over the observed large and small area until 20:00:00 UTC on the 30 July (Fig. 4.2 - C, D). However, while the mélange has generally similar velocities throughout it does not necessarily mean that the mélange lacked motion.

4.2.3 *OpenPIV*

Using openPIV in Python, multi-look intensity image frames are cross-correlated with a 550 x 550 m interrogation window and 450 x 450 m overlap to feature track and create velocity vector maps monitoring mélange behavior. A velocity map taken between 04:00:00 UTC and 05:00:00 UTC on 29 July coincides with the last of the tsunamic waves created by the third calving event (Fig. 4.3 – A). During this time, the loose icebergs and developing mélange were pushed back on the terminus ice by the waves created by the calving event. The temporary jamming of sea ice and icebergs on the ice tooth is synchronous with the deceleration of the ice tooth. An openPIV vector map between 05:00:00 and 06:00:00 UTC show the serac event that caused a large mélange velocity up until around 08:00:00 UTC when the developing mélange begins to harden (Fig. 4.3 – B). Once the mélange begins to form, multi-look intensity images taken in hourly intervals show little to no movement at distances 3.16 km from the terminus until 21:00:00 UTC 30 July when the mélange begins to disintegrate.

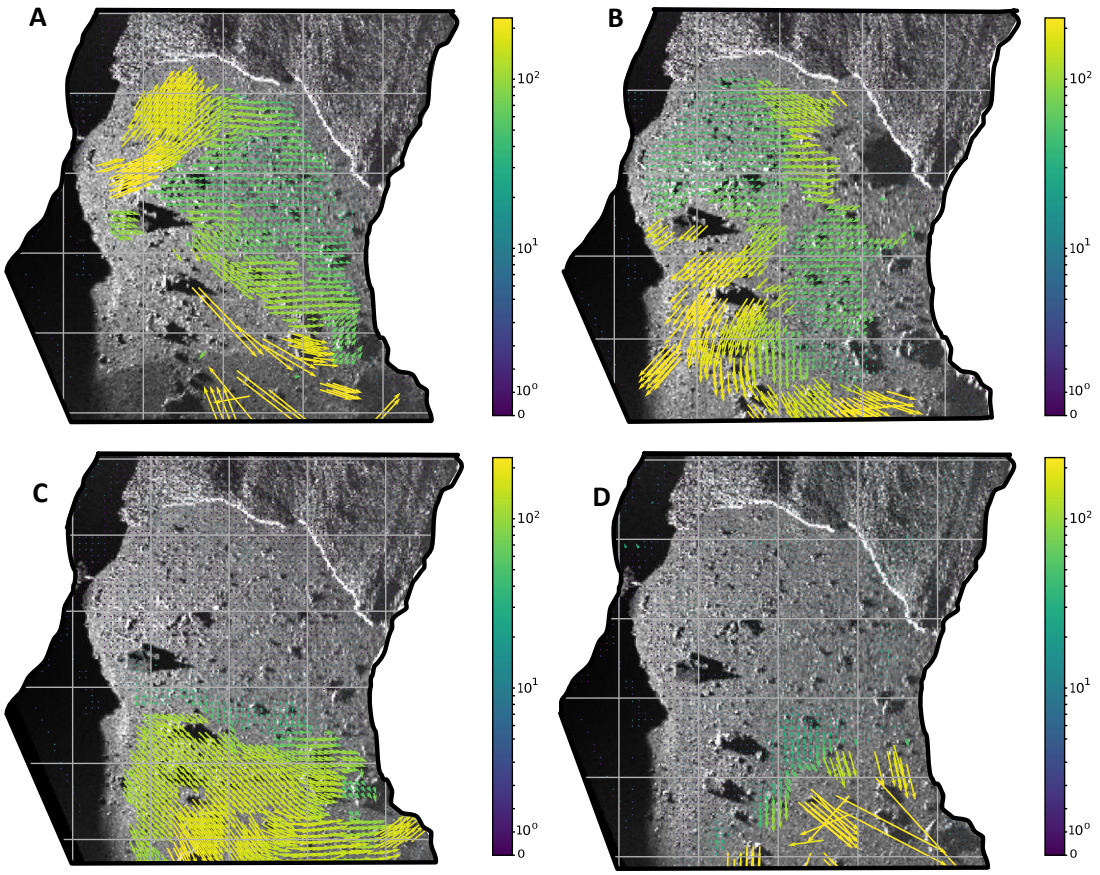

Figure 4.3. An openPIV vector map superimposed on multi-look intensity images that coordinate with vector times. Arrows indicate direction and magnitude of interpreted movement on a logarithmic color scale. Areas with dots indicate little to no motion in that area. A) From 04:00:00 and 05:00:00 UTC on 29 July. At this time, seen in the velocity vectors, calved ice is moving backward and is jamming up on the terminus. B) From 05:00:00 and 06:00:00 UTC on 29 July. C) From 08:00:00 and 09:00:00 UTC on 29 July. The lack of motion near the terminus indicates mélange rigidity. D) From 11:00:00 and 12:00:00 UTC on 29 July.

4.3 Rift Displacement

As the ice tooth began to accelerate after the second calving event, the force from the calving iceberg opened a rift between the ice tooth and glacier. To determine how much the rift was torn open and then partially closed after the calving event, I use the same green and black velocities from Figure 4.1 and create a 1.5-hour running average time series of velocity at those positions (Fig. 4.4 – C). After creating a time series of speed, I calculate the total displacement of the rift by multiplying the running average velocities by the time between each sample, 2.5 minutes, and then divided by 1440, the number of minutes in a day. I calculated a total displacement as a function of time by adding each subsequent displacement to the value beforehand. I then detrend the data by subtracting an ordinary linear least-squares regression line for the

cumulative mean displacement to show the approximate dislocation of the ice tooth. I plot the ice tooth's detrended displacement against the displacement of glacier ice on the other side of the rifted opening (Fig. 4.4). The displacement begins at zero, but doesn't necessarily mean that the rift was completely closed to begin with; just that we start summing up the displacement at that junction in time.

The opening of the rift between the ice tooth and glacier illustrates the deformation caused by the force of the calving iceberg. Leading up to the third calving event the surface rift between the ice tooth and glacier locally opened about 1 to 1.3 m before starting to partially close after the calving event. The tip of the ice tooth rotated further from the glacier than the ice further away because it was more directly connected to the calving iceberg. After calving, both rifted areas started to partially close as mélange developed and hardened in the fjord until around the time that mélange began to disintegrate the 30 July. Around the time the mélange begins to disintegrate (Section 4.2), the distance between the ice tooth and glacier stays constant (Fig. 4.4). The timing of the partial closing of the ice tooth's rift coincides with the introduction of icebergs and strengthening of the developing mélange in the fjord.

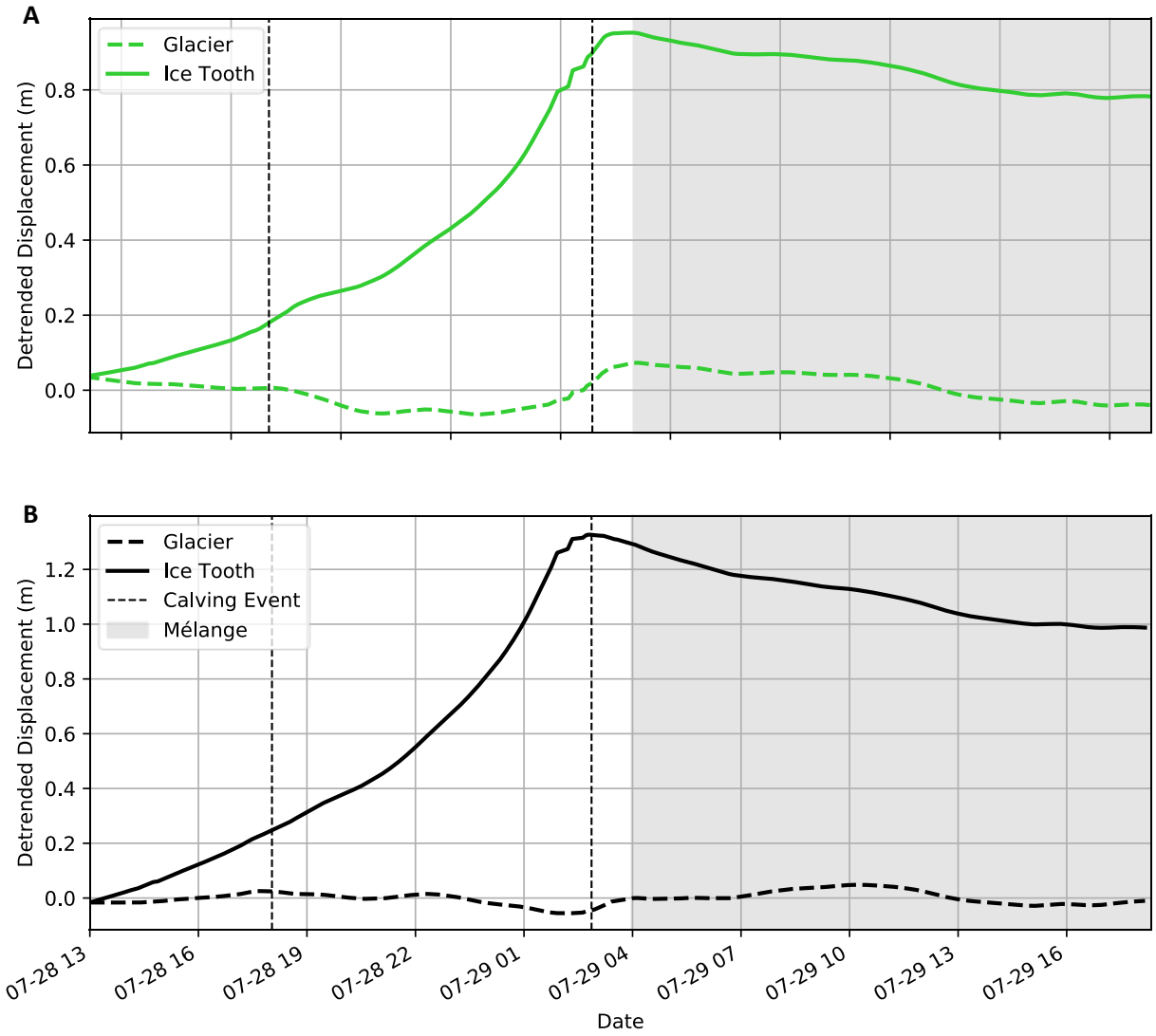

Figure 4.4. Rift displacement time series at two ice tooth (inverted triangles) and two glacier (squares) positions from Figure 4.1. A) Lime green rift displacement between the glacier and ice tooth. B) Black rift displacement between the glacier and the tip of the ice tooth

5. Discussion

Occurrences of transitory, summer mélange is an important consideration when analyzing calving behavior and glacier dynamics. Here, I have shown that mélange can influence calving and glacier behavior through 1) ocean waves compressing nearby mélange onto the ice tooth after calving, and 2) stabilization the ice tooth through the strength of mélange's ice-to-fjord contact at the shear margins, at least until the mélange loses its rigidity and circulates away from the terminus.

5.2 Mélange and Glacier Response

While mélange composition and rheology can vary greatly, here summer mélange develops following slab capsizing calving events where the icebergs fractured into many pieces, were distributed throughout fjord, formed mélange, and after a day and a half circulated away from the fjord. As the shattered icebergs circulated throughout the fjord, waves created by the calving event directed calved ice back onto the calving front at the same time that the ice tooth reached its slowest velocity at the front tip of the ice tooth (Fig. 4.1, 4.2). This suggests that the force of the mélange and newly introduced icebergs created some compressional stress on the ice tooth. Additionally, the ice tooth was consistently slower than the glacier until the mélange lost its rigidity, suggesting that the mélange has some resistive strength. Meanwhile, the fully-attached glacier ice did not decelerate or have a substantial velocity change at any point when the mélange was forming, indicating that while there is a certain amount of pressure exerted by the mélange, it is not enough to impact the flow of the entire glacier front.

The summer mélange experienced repeated fracturing, jamming, and refreezing while the mélange was present, but lateral drag at the fjord walls and poor ocean circulation kept the line-of-sight velocity of mélange relatively steady until late on the 30 July (Fig. 4.2). We conclude that summer mélange may influence the motion of terminus ice. Depending on the frequency of summer mélange and availability of rifting ice, this type of short-lived mélange may influence the timing of some calving events and alter terminus geometries over the course of a summer.

5.3 Forces and Shear Stress on Calving Iceberg

5.3.1 Force Balance Setup

Determining shear stresses and fracture behavior of ice is relevant to understanding glacier and ice sheet mechanics. I find the shear strength of terminus ice at Rink Isbrae by creating a simple force balance analysis similar to work by MacAyeal and others (2003), Tsai and others (2008), Amundson and others (2010, 2012), and Burton and others (2012) where they analyze the capsize trajectory of an iceberg floating in the fjord waters and leaning on the terminus. However, unlike their models, this iceberg is mechanically

connected to the glacier through its attachment to the ice tooth, and the iceberg is fixed on the glacier at a hinge point (Fig. 5.1 - A).

I approximate the calving iceberg as a rectangular prism because it has been shown that full-thickness calved icebergs adhere to rectangular geometries in prior research (Walter and others, 2012; Burton and others, 2012). The surface dimensions of the iceberg are drawn from shadows cast on the glacier in multi-look intensity images from iceberg rotation and assumed basal crevasse propagation (Fig. 5.1 – A), the ice thicknesses were drawn from BedMachine data (Morlighem and others, 2017), and approximate elevations are taken from buoyantly flexing icebergs in ArcticDEM (Porter and others, 2018) at Rink Isbrae. BedMachine data comes from a radar-derived ice thickness project aimed to compile data on Greenland's bed topography, seafloor bathymetry, and ice thickness through a mass conservation approach. BedMachine data's datum is relative to the geoid of the Earth in meters above mean sea level, which does not need to be corrected for. ArcticDEM surface elevations use WGS84 datum relative to the ellipsoid of the earth which is 31.657 m above the geoid. I correct ArcticDEM surface elevations to reflect the geoids heights by subtracting ArcticDEM surface elevations by the geoid height.

The forces on the iceberg are the positive upward buoyant force F_b, the negative downward gravitational weight F_g of the iceberg, and the downward contact force F_c of the iceberg held against the glacier. When the iceberg is held statically by the glacier ice until the initiation of calving where the iceberg starts to accelerate all of these forces summed together equal the net force, and this net force should sum to zero, F_{net}. Using Figure 5.1 as a visual tool, the forces are described as:

$$F_{net} = 0 = F_b + F_g + F_c \qquad (4)$$

$$F_b = \rho_w g V_s \qquad (5)$$

$$F_g = -\rho_i g V_i \qquad (6)$$

$$F_c = -(F_b + F_g) \qquad (7)$$

where ρ_w is the density of sea water, ρ_i is the density of ice, g is gravitational acceleration, V_i is the volume of the whole iceberg, and V_s is the volume of the submerged portion of iceberg (e.g. Table 5.1). The contact force is the force holding the iceberg to the glacier and is between the ice tooth and third iceberg (Fig. 5.1 – A (yellow)) and it is a function of the rotation of the iceberg. If the contact force is negative, the buoyancy force is greater than the force of gravity, and if the contact force is positive, then the force of

gravity is greater than the force of buoyancy. Since the iceberg is in static equilibrium there are no drag forces that need to be considered.

To determine the forces acting on the iceberg, the angle of rotation (θ) right before calving must be found (Fig. 5.1 – B). First, I find the distance between the radar and the glacier position where the shadow stops $\overrightarrow{ab}$ (5700 m), and I use that distance calculate the angle between the radar and the terminus ice (α) with surface elevation data from field collection a (427 m) and ArcticDEM data b at Rink Isbrae from 28 May, 2014. I then determine the average glacier slope angle using surface elevations from ArticDEM data at Rink Isbrae's terminus (β).

Table 5.1 **Physical Parameters Used in Calculations**	
Parameter	Value
Average ice thickness H	450 – 600 m
Average ice thickness H_t at ice tooth	460 m
Iceberg width W at shadow	230 m
Iceberg width W_t at ice tooth	400 m
Iceberg length L	1340 m
Far shadow elevation b	31 m
Hinge elevation c	22 m
Horizontal distance of shadow $\overrightarrow{bc}$	75 m
Gravitational acceleration g	9.8 m/s^2
Density of ice ρ_i	917 kg/m^3
Density of sea water ρ_w	1,020 kg/m^3

$$\tan^{-1}\left(\frac{a-b}{\overrightarrow{ab}}\right) = \alpha \qquad (8)$$

$$\tan^{-1}\left(\frac{b-c}{\overrightarrow{bc}}\right) = \beta \qquad (9)$$

where c is the surface elevation at the terminus that isn't on the iceberg and $\overrightarrow{bc}$ is the horizontal distance between b and c taken from multi-look intensity images. Together, the iceberg-grazing radar look angle and the surface slope of the glacier are summed and give the angle δ:

$$\delta = \alpha + \beta \qquad (10)$$

The vertical change at the point of flexure between the iceberg and glacier at c and top of the radar-grazing shadow B is found by:

$$B = \sin\delta \cdot \overrightarrow{bc} \qquad (11)$$

I then calculate the angle of flexure between the glacier and the far, highest elevated corner of the rotating iceberg by finding (γ) and (ζ) as:

$$\gamma = 180° - 90° - \delta \qquad (12)$$

$$\zeta = \cos^{-1}\left(\frac{B}{W}\right) \qquad (13)$$

where W is the width of the iceberg at the shadow (Table 5.1). From here, θ can be calculated as:

$$\theta = 180 - \zeta - \gamma \qquad (14)$$

where θ is estimated to be ~14°. Using θ, I find the areas of the whole iceberg and the submerged portion of iceberg to determine the volumes for the force balance equations. To find the areas of the iceberg (Fig. 5.1 – C) I must find the freeboard lengths ($C_{1,2,3}$), which are side lengths of the iceberg above the water. The freeboard lengths are found by:

$$C_1 = \tan\theta\, W \qquad (15)$$

$$C_2 = \tan\Psi\, W \qquad (16)$$

where C_1 is the length of the iceberg facing the ocean tipping out of the water, C_2 is a portion of the C_1 length used to separate the aerial portions of iceberg into a rectangle and triangle, and Ψ is the angle difference between θ and β (Fig 5.1 – C). Here, I find the inner length of the aerial portion of iceberg C_3 as:

$$C_3 = C_1 - C_2 \qquad (17)$$

I then find the areas of the iceberg face as:

$$A_1 = \left(\frac{1}{2}\right) C_2 \, W \qquad (18)$$

$$A_2 = C_3 \, W \qquad (19)$$

where A_1 is the area of the small triangle and A_2 is the area of the rectangle above the triangle that is attached to the glacier Figure 5.1 – C. I then calculate iceberg volumes as:

$$V_i = LWH \qquad (20)$$

$$V_s = V_i \; - \; (A_1 + A_2)L \qquad (21)$$

where *L* is iceberg length and H are average ice thicknesses (Table 5.1). The volume equations (20 and 21) can now be plugged back into the force equations (5 and 6) and the contact force (7) can be quantified. For the given range of iceberg thicknesses, I estimate a contact force between $-7.7 * 10^9 \, N$ to $-8.4 * 10^{10} \, N$. The contact force is negative when buoyancy is greater than the force of gravity and because equation 7 is even though the iceberg is being forced upward.

5.3.2 Shear Strength of Ice

To find the maximum shear stress or shear strength of ice between the iceberg and adjacent ice tooth at calving, we take the contact force (eqn. 7) divide it over the estimated area of contact (Fig. 5.1 - A):

$$A \; = \; W_t \, * \, H_t \qquad (22)$$

$$\sigma_{max} = \frac{F_c}{A} \qquad (23)$$

where A is the contact area between the iceberg and ice tooth and σ_{max} is the shear stress right before calving. Once the maximum shear stress of the terminus ice is exceeded, the shear strength is reached, and calving occurs. I estimate the shear strength of terminus ice to fall between $50 \, kPa$ to $540 \, kPa$ (Fig. 5.2). The shear strength should increase with iceberg height because shear stresses increase as a glacier thickens (Ma and others, 2017).

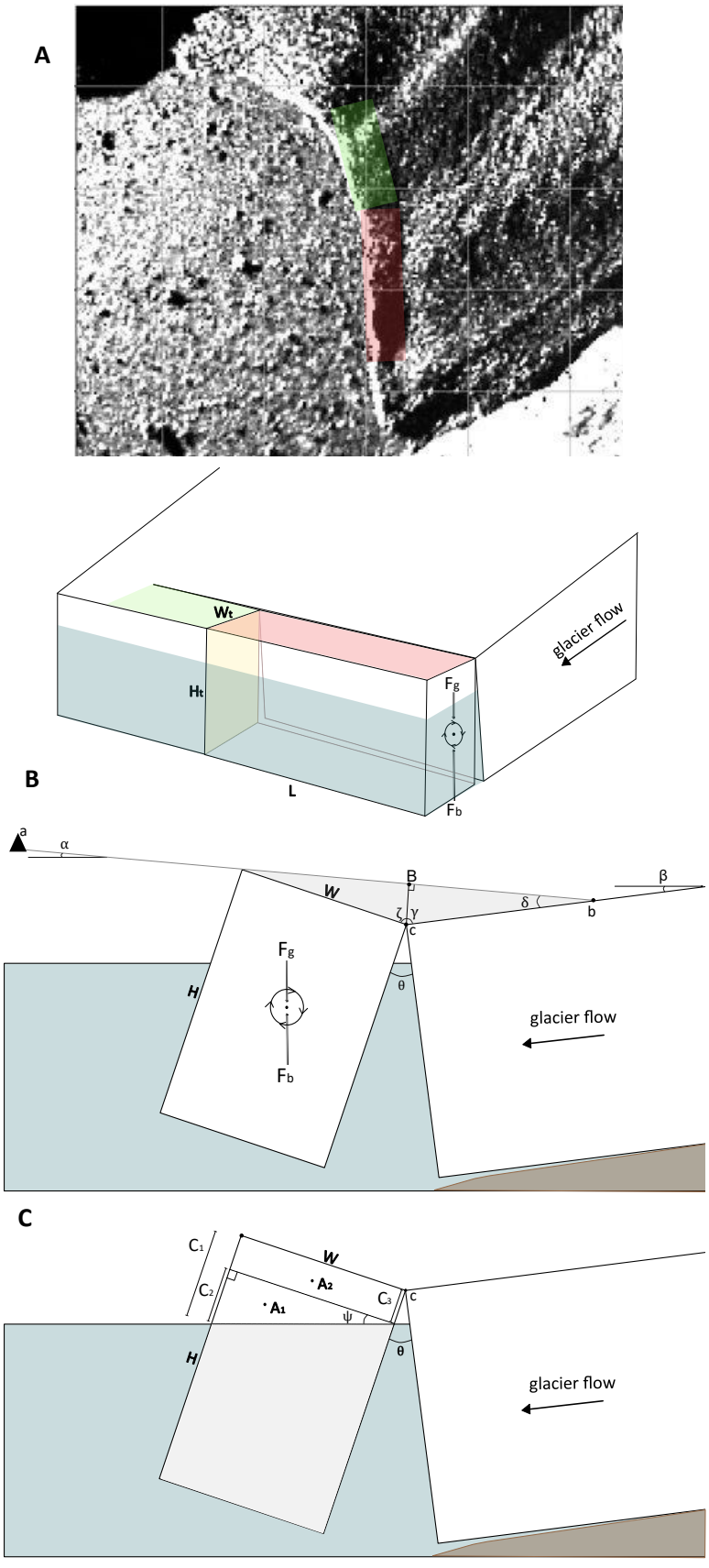

Figure 5.1. Schematic diagrams of iceberg cross sections. (A) A reference multi-look intensity image on glacier of iceberg (red) and ice tooth (green). A not-to-scale 3-D diagram of the rotating iceberg (red), connected ice tooth (green), area of shear failure between the ice tooth and iceberg also F_c (yellow), and B) Exaggerated 2-D model of distances, forces, and angles needed to calculate the iceberg's rotational angle (θ). The black rectangle (A) represents the terrestrial radar interferometer, the shadowed triangle represents the depression in the MLI in part A to get the iceberg dimensions. C) 2-D model of freeboard lengths ($C_{1,2,3}$) used to get A_1 and A_2 which are used to calculate the iceberg's whole and submerged volume (see section 5.2.1).

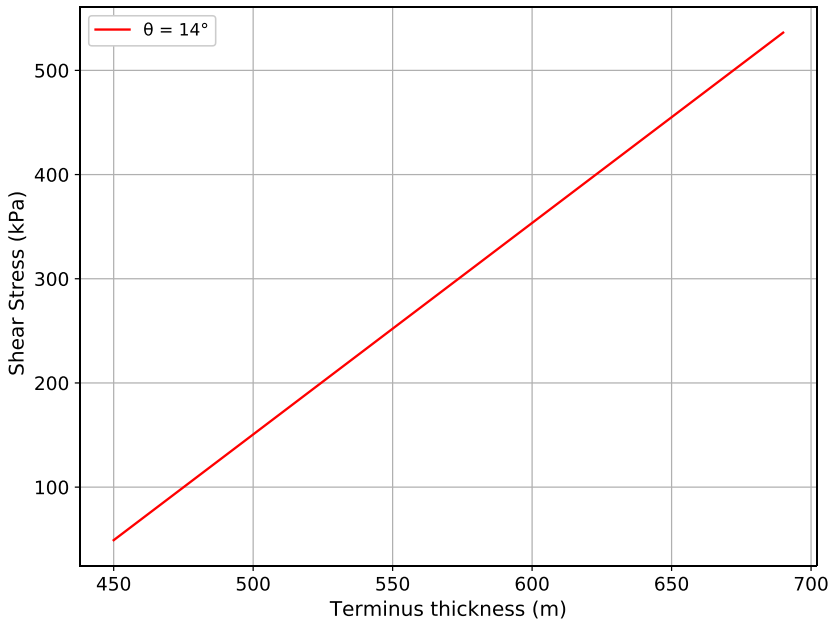

Figure 5.2. Shear stress on the iceberg at with varying iceberg thicknesses at calving when $\theta = 14°$. Therefore, shear strength of ice in this study is found between 50 kPa and 540 kPa.

Information on ice shear strength has historically been a difficult property to measure and is not well constrained. Early laboratory work on the shear strength of fresh lake ice was estimated between 410 to 820 kPa (Wilson and Horeth, 1948). Another study using simple beam theory and finite element analysis found that the shear strength of ice fell between 0.3 and 1.6 MPa depending on ice beam loads and saw cut shapes (Frederking and others, 1988). An experiment using a four-point beam bending trial found that the shear strength of glacial ice in Greenland was between 0.2 to 1.5 MPa (Gagnon and Gammon, 1995). In another study, for freshwater ice temperatures varying from -5° to -60°C, the shear strength of ice was measured to fall between 0.5 and 1.2 MPa (Bragov and others, 2015). While our calculated values are somewhat lower than those reported in the literature, these values are based on our field observations at Rink Isbrae and may be more representative of the in-situ properties of actual tidewater glaciers than earlier measurements developed from models or measured under ideal conditions.

Employing realistic shear strengths of glacier ice to ice sheet modelling is essential for examining full stress regimes across a glacier and predicting fracture behavior leading to full-thickness calving events. The estimated shear strength for Rink Isbrae's terminus is on the low end of some earlier approximations. These values may be explained by the highly crevassed nature of the terminus, which has been shown to lower stress approximations (Vaughn, 1993). Recently, shear failure has been proposed to be as influential to crevasse propagation and calving as tensile and compressive failure (Bassis and Walker, 2012), which has

been projected to occur at stresses between $0.7 - 3.1\ MPa$ and $5 - 25\ MPa$, respectively (Petrovic, 2003). Additionally, shear failure at Rink Isbrae through slab capsize calving seems create a domino effect where one calving event tears the ice laterally connected to it which triggers more calving (ex. Fig. 5.3). The lateral tearing of the iceberg from the glacier may increase the chances of slab capsize style calving which induces shear failure somewhere along the rifting iceberg. Since slab capsize calving is a dominant mode of calving at tidewater glaciers, shear failure glacier termini may contribute more to calving behavior than previously appreciated. Therefore, it is important to consider lateral tearing processes that influence calving as well.

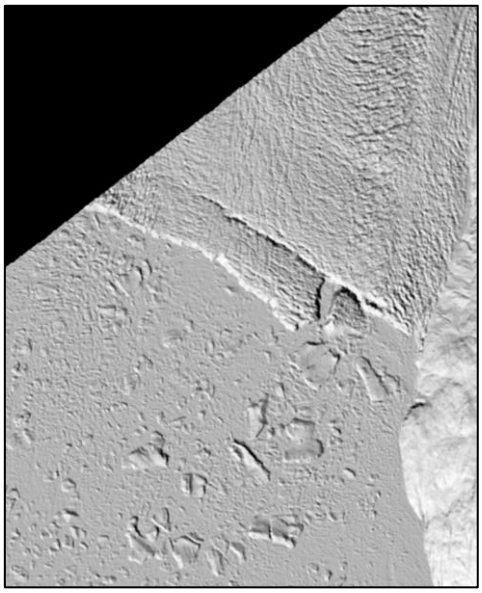

Figure 5.3. Arctic Polar Stereographic image from ArticDEM of a rifting piece of terminus ice from 9 April, 2013, at Rink Isbrae, West Greenland.

5.4 Rift Displacement

After the calving event, the mélange had enough strength to stabilize the ice tooth and slow it down while the up-glacier ice flowed forward to partially close the rifted gap. The gradient in velocity on the ice tooth implies that the compressibility of the ice is enough to accommodate the imposed stress on the ice tooth. The ice tooth remained on the terminus until it calved sometime between August 4nd and 7th in 2014 as seen in Landsat 8 data from Google Earth Engine (Gorelick and others, 2017).

5.5 Other Summer Mélange Occurrences

Summer mélange development following slab capsizing events are not isolated occurrences unique to Rink Isbræ (Fig. 5.4). Using Landsat satellite imagery, I observed 24 tidewater glaciers around Greenland

between 2000 and 2019 through the months of May and November to gain a more comprehensive understanding of summer mélange occurrences (Lea, 2018). I found that outlet glaciers at all latitudes in Greenland occasionally develop mélange following predominately slab capsize calving events (Table 5.2). I observed mélange in fjords did not continuously have mélange present in the fjord throughout the year (i.e. Jakobshavn Isbrae, Helheim Glacier (Fig. 5.4 – G), Kangerlussuaq Glacier, etc.), were in semi-confined (at least 2 km distance from open ocean) to confined fjords (greater than 2 km from open ocean), the mélange was connected to the terminus, had many distributed icebergs, and showed some fracturing within the sea ice to suggest some rigidity.

When summer mélange occurred, depending on location on the Greenland Ice Sheet, it would occur once or twice in a season and would last several days to several weeks in front of a terminus. However, summer mélange did not occur every year at some glaciers that may have experienced summer melange the previous year. Periods of summer mélange formed in late July to August at glaciers on the western side of Greenland, late August to early October for northwestern glaciers, mid-September to October for northern glaciers, early June through late October for southern glaciers, and late July to November for some glaciers on the eastern and southeastern portion of Greenland. Terminus length and fjord confinement was not as influential as the style of calving to initiate mélange development (Table 5.2). The mélange usually followed larger calving events where icebergs broke apart due to extensive crevassing induced by longitudinal stretching. Some glaciers, like Alison Glacier, West Greenland and Daugaard-Jensen, East Greenland, had many calving episodes in the summer that often create intense amounts of summer mélange with high iceberg density, which rarely became detached from the terminus. Mélange with fewer icebergs produced at smaller glaciers lasted for several days before disintegrating. The extent of summer mélange at outlet glaciers in Greenland is not limited by latitude and is most likely controlled by fjord geometry, horizontal wind circulation, iceberg density, and calving style.

Table 5.2. List of Greenland outlet glaciers observed for summer mélange development between 2000 and 2019 in Landsat imagery. One checkmark in the mélange category means that there were periodic summer mélange occurrences. Two checkmarks in the mélange category means that the respective glacier had persistent mélange all year. No checkmarks indicate that mélange would never form beyond sea ice in the winter.

Location	Glacier	Fjord width (km)	Summer mélange?	Dominant calving style	Mélange Months	Fjord confinement
Central West	Rink Isbræ	~ 4.5 km	✓	Slab capsize, tabular	July - Sept	Confined
Central West	Kangerdludssup Sermesua	~ 4 km	N/A	Tabular, serac		Confined

Central West	Sermeq Silarleq	~ 3.5 km	✓	Slab capsize	July - Sept	Confined
Central West	Kangigleq	~ 4.7 km	N/A	Serac		Confined
Central West	Sermilik	~ 2.7 km	N/A	Serac		Confined
Central West	Lille	~ 2 km	N/A	Serac		Confined
Central West	Store	~ 5.4 km	✓	Slab capsize, tabular	July - Oct	Confined
Northwest	Upernavik Isstrom	~ 4 km (trunk dependence)	✓✓	Slab capsize, tabular	Aug- Oct	Semi-confined
Northwest	Ingia Isbræ	~ 3.7 km	✓	Slab capsize, tabular	July - Sept	Confined
Northwest	Alison	~ 4.8 km	✓✓	Slab capsize, tabular, rifting	Aug- Oct (early 2000s)	Semi-confined
Northwest	Ilulip	~ 5.1 km	✓	Slab capsize, tabular	Aug- Oct	Semi-confined
Northwest	Kong Oscar	~ 4.2 km	✓	Slab capsize, tabular	Aug - Sept	Semi-confined
Northwest	Sverdrup	~ 3.5 km	✓✓	Slab capsize, tabular	Sept - Oct	Semi-confined
Northwest	Gada	~ 2 km	✓	Slab capsize	Late Aug - October	Semi - confined
North	Ostenfeld	~ 5.6 km	N/A	Tabular		Confined
North	Steensby	~ 5.1 km	N/A	Tabular		Confined
North	Tracy	~ 4 km	✓	Slab capsize, tabular	Late Aug - Sept	Semi-confined
Northeast	Zachariae	~ 5.1 km	N/A	Tabular, rifting		Semi - confined
Central East	Kong Christian VI	~ 7.6 km	N/A	Slab capsize, serac		Semi-confined
Central East	Kronborg	~ 2.7 km	✓	Slab capsize, serac	July- Sept	Semi-confined
Central East	Storbrae N	~ 2.1 km	✓	Slab capsize	July	Confined
Central East	Daugaard-Jensen	~ 6.2 km	✓✓	Slab capsize, tabular	Aug – Sept	Confined
Southwest	Kangilemgata Sermia	~ 4.3 km	✓	Slab capsize	Late July - Oct	Confined
Southeast	Fimbul	~ 4 km	✓✓	Slab capsize	Sept - Nov	Confined

Winter mélange has been observed to be disintegrating earlier in the year at multiple outlet glaciers around Greenland, and with the potential decline of winter mélange at glacier termini, frequency of calving may increase which may intensify the presence of summer mélange. The impact of summer mélange may be greater than currently valued. Summer mélange occurrences around Greenland could become more important since seasonal mélange and sea ice has been disintegrating earlier in the year and the duration of when strong calving occurs has increased (Joughin and others, 2012). To understand mélange's complete influence on calving behavior and glacier evolution, determining which tidewater glaciers can develop a summer mélange is imperative. In addition to isolating occurrences of potentially impactful mélange, quantifying mélange rheology and strength in various glacial systems is also important to the glaciologic community.

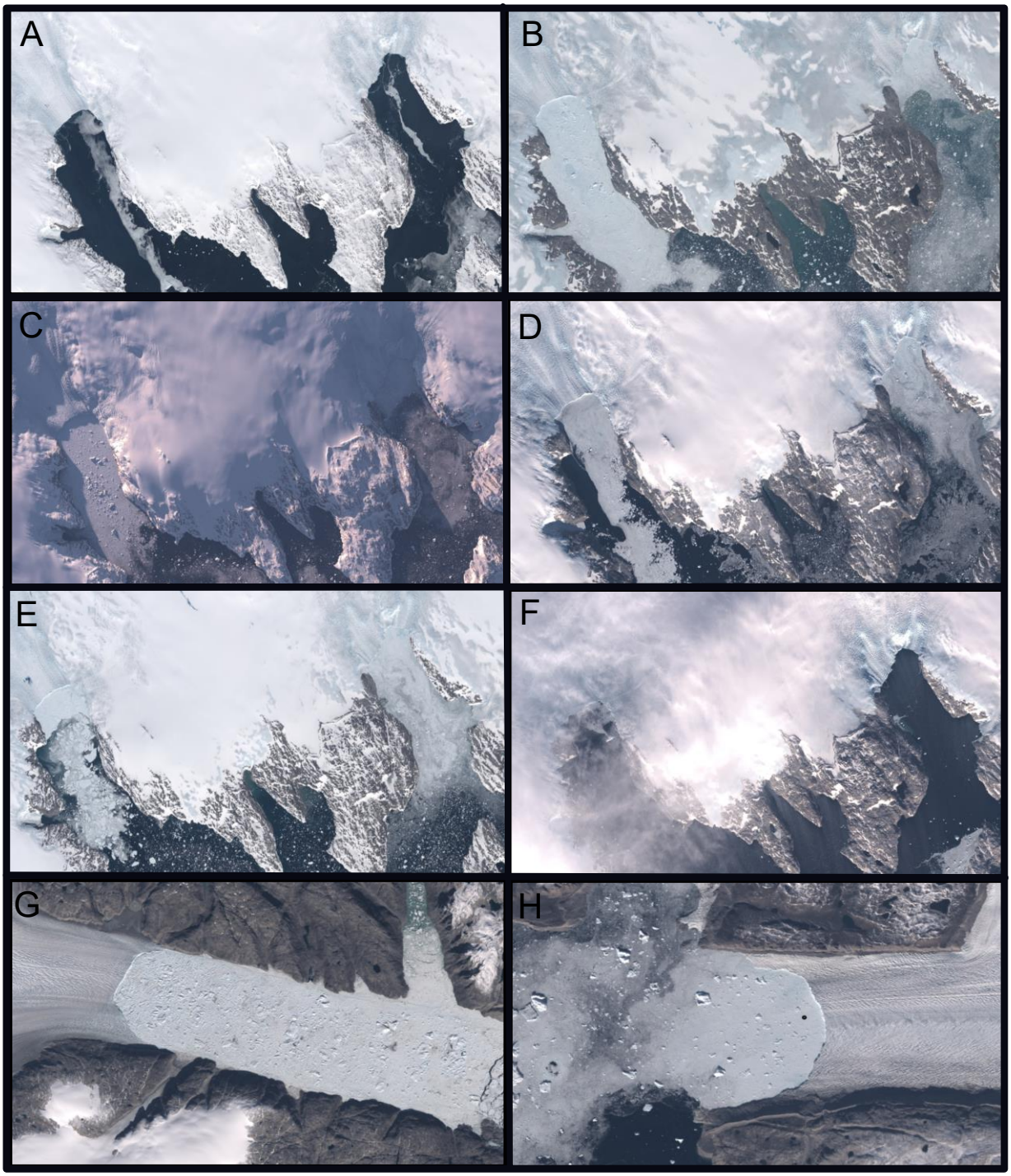

Figure 5.4. Images are from Google Earth Engine Digitization Tool v1.012 (Lea, 2018). A – F) Instance of temporary, summer mélange at two fast flowing glaciers, Køge Bugt Glacier (left) and Pamiagtik Glacier in Køge Bugt Ikeq embayment, in Southeast Greenland. In (A – 9 June, 2014) there is no mélange present and as a result of calving events, mélange develops and remains in front of the fjords until (E – 15 October, 2014). By 24 October, 2014, the icebergs are completely gone from both glacier fronts. G) Instance of permenant, year-round mélange at Helheim Glacier, Southeast Greenland. H) Instance of ice discharge in front of Tracy Glacier that does not harden into a mélange.

6. Conclusion

Summer mélange can impact glacier dynamics at Greenland's tidewater glaciers. In this study, I observed three separate, large calving events at Rink Isbræ followed by mélange development with terrestrial radar interferometry to analyze mélange influence on a glacier terminus and estimate the shear strength of ice during slab capsize calving. The summer mélange exerts resistive stresses on the terminus by compressing recently calved icebergs onto a rifting ice tooth and through the mélanges' ice-to-ice and ice-to-rock interactions at the shear margins of the fjord. The mélange can influence fractured, fragile portions of terminus ice, like the ice tooth, by briefly stabilizing the rifted ice and likely delaying the timing of calving. However, the glacier immediately behind the large-scale rifts was not detectably influenced by the temporary mélange formation. If winter mélange continues to disintegrate earlier in the summer months as projected (Joughin and others, 2008; Joughin and others, 2012), summer mélange may become more important to understanding dynamic shifts in tidewater glacier evolution.

The shear strength of ice during this calving event was estimated to be $50\ kPa$ to $540\ kPa$, which helps constrain the strength of terminus ice to be a lower value than previously considered and is representative of actual shear strengths estimated at a glacier terminus. Additionally, slab capsize style calving can produce an avalanche effect at the terminus where one calving event tears adjacent ice away from the glacier which generates more calving. This phenomena may occur at other glaciers similar to Rink Isbrae. For instance, in James and others (2014) study of Helheim Glacier, there is a slab capsizing event appears to have a similar ice tooth that may be impacted by the year-round mélange that occurs at Helheim Glacier.

This study provides insight into the magnitude of mélange impact and the shear strength of Rink Isbrae's terminus ice in the process of calving. If winter mélange and constant, year-round mélange can slow a tidewater glacier by allowing thickening and advancement of the grounding line, inhibiting calving, and stabilizing the calving front, in what ways will ephemeral, likely thinner summer mélange influence evolving terminus stability? As the major outlet glaciers in Greenland, like Rink Isbrae, continue to melt, calve, and evolve, quantifying mélange variability and the shear strength of terminus ice as a feedback to calving is imperative to understand. Additional work on mélange and the shear strength of ice at glacier termini may provide insight into how Greenland will be responding as the global climate continues to warm, how much ice volume will be lost from the Greenland Ice Sheet, and how is sea level likely to rise in the coming century.

7.0 Bibliography

Amaral, T., Bartholomaus, T. C., & Enderlin, E. M. (2020). Evaluation of iceberg calving models against observations from Greenland outlet glaciers. *Journal of Geophysical Research: Earth Surface*, 125. https://doi.org/ 10.1029/2019JF005444

Amundson, J. M., & Burton, J. C. (2018). Quasi-Static Granular Flow of Ice Mélange. *Journal of Geophysical Research: Earth Surface*, *123*(9), 2243–2257. https://doi.org/10.1029/2018JF004685

Amundson, J. M., Fahnestock, M., Truffer, M., Brown, J., Lüthi, M. P., & Motyka, R. J. (2010). Ice mélange dynamics and implications for terminus stability, Jakobshavn Isbrse, Greenland. *Journal of Geophysical Research: Earth Surface*, *115*(1), 1–12. https://doi.org/10.1029/2009JF001405

Amundson, Jason M., Clinton, J. F., Fahnestock, M., Truffer, M., Lüthi, M. P., & Motyka, R. J. (2012). Observing calving-generated ocean waves with coastal broadband seismometers, jakobshavn isbræ, greenland. *Annals of Glaciology*, *53*(60), 79–84. https://doi.org/10.3189/2012/AoG60A200

Amundson, Jason M, Kienholz, C., Hager, A. O., Jackson, R. H., Motyka, R. J., Sutherland, D. A., & Nash, J. D. (2020). Formation , flow and break-up of ephemeral ice mélange at LeConte Glacier and Bay , Alaska, 1–14.

Andersen, M. L., Stenseng, L., Skourup, H., Colgan, W., Khan, S. A., Kristensen, S. S., et al. (2015). Basin-scale partitioning of Greenland ice sheet mass balance components (2007-2011). *Earth and Planetary Science Letters*, *409*, 89–95. https://doi.org/10.1016/j.epsl.2014.10.015

Aström, J. A., Vallot, D., Schäfer, M., Welty, E. Z., O'Neel, S., Bartholomaus, T. C., et al. (2014). Termini of calving glaciers as self-organized critical systems. *Nature Geoscience*, *7*(12), 874–878. https://doi.org/10.1038/ngeo2290

Bartholomaus, T. C., Larsen, C. F., & O'Neel, S. (2013). Does calving matter? Evidence for significant submarine melt. *Earth and Planetary Science Letters*. https://doi.org/10.1016/j.epsl.2013.08.014

Bassis, J. N., & Jacobs, S. (2013). Diverse calving patterns linked to glacier geometry. *Nature Geoscience*, *6*(10), 833–836. https://doi.org/10.1038/ngeo1887

Bassis, J. N., & Walker, C. C. (2012). Upper and lower limits on the stability of calving glaciers from the yield strength envelope of ice. *Proceedings of the Royal Society A: Mathematical, Physical and Engineering Sciences*, *468*(2140), 913–931. https://doi.org/10.1098/rspa.2011.0422

Benn, D. I., Hulton, N. R. J., & Mottram, R. H. (2007). "Calving laws", "sliding laws" and the stability of tidewater glaciers. In *Annals of Glaciology*. https://doi.org/10.3189/172756407782871161

Benn, D. I., Cowton, T., Todd, J., & Luckman, A. (2017). Glacier Calving in Greenland. *Current Climate Change Reports*. https://doi.org/10.1007/s40641-017-0070-1

Benn, D. I., Åström, J. A. N., Zwinger, T., Todd, J. O. E., Nick, F. M., Cook, S., et al. (2017). Melt-under-cutting and buoyancy-driven calving from tidewater glaciers : new insights from discrete element and continuum model simulations, *63*, 691–702. https://doi.org/10.1017/jog.2017.41

Box, J. E., & Steffen, K. (2001). on the Greenland ice sheet from automated station observations x 1014 kg yr profile method and kg yr - for rates were. *Network*, *106*(July 1991), 965–981. https://doi.org/10.1029/2001JD900219

Bragov, A., Igumnov, L., Konstantinov, A., Lomunov, A., Filippov, A., Shmotin, Y., et al. (2015). Investigation of strength properties of freshwater ice. *EPJ Web of Conferences*, *94*, 1–5.

https://doi.org/10.1051/epjconf/20159401070

Van Den Broeke, M., Bamber, J., Ettema, J., Rignot, E., Schrama, E., Van Berg, W. J. De, et al. (2009). Partitioning recent Greenland mass loss. *Science*, *326*(5955), 984–986. https://doi.org/10.1126/science.1178176

Burton, J. C., Amundson, J. M., Abbot, D. S., Boghosian, A., Cathles, L. M., Correa-Legisos, S., et al. (2012). Laboratory investigations of iceberg capsize dynamics, energy dissipation and tsunamigenesis. *Journal of Geophysical Research: Earth Surface*, *117*(1), 1–13. https://doi.org/10.1029/2011JF002055

Burton, Justin C, Amundson, J. M., Cassotto, R., Kuo, C., & Dennin, M. (2018). Quantifying flow and stress in ice m elange , the world ' s largest granular material, *115*(20), 5105–5110. https://doi.org/10.1073/pnas.1715136115

Caduff, R., Schlunegger, F., Kos, A., & Wiesmann, A. (2015). A review of terrestrial radar interferometry for measuring surface change in the geosciences, *228*(October 2014), 208–228. https://doi.org/10.1002/esp.3656

Cassotto, R., Fahnestock, M., Amundson, J. M., Truffer, M., & Joughin, I. (2015). Seasonal and interannual variations in ice mélange and its impact on terminus stability, Jakobshavn Isbræ, Greenland. *Journal of Glaciology*, *61*(225). https://doi.org/10.3189/2015JoG13J235

Cassotto, R., Fahnestock, M., Amundson, J. M., Truffer, M., Boettcher, M. S., De La Peña, S., & Howat, I. (2019). Non-linear glacier response to calving events, Jakobshavn Isbræ, Greenland. *Journal of Glaciology*, *65*(249), 39–54. https://doi.org/10.1017/jog.2018.90

Colgan, W., Rajaram, H., Abdalati, W., Mccutchan, C., Mottram, R., Moussavi, M. S., & Grigsby, S. (2016). Glacier crevasses: Observations, models, and mass balance implications. *Reviews of Geophysics*, *54*, 119–161. https://doi.org/10.1002/2015RG000504.

Croutch, V. K.; Hartley, R. A. Adhesion of Ice to Coatings and the Performance of Ice Release Coatings. J. Coatings Technol.1992, 64, 41–53

Dixon, T. H., Voytenko, D., Lembke, C., De La Pea, S., Howat, I., Gourmelen, N., et al. (2012). Emerging technology monitors ice-sea interface at outlet glaciers. *Eos*, *93*(48), 497–498. https://doi.org/10.1029/2012EO480001

Enderlin, E., Howat, I., Jeong, S., Noh, M.-Jo., Angelen, J., & van den Broeke, M. (2014). An improved mass budget for the Greenland ice sheet. *Geophysical Research Letters*, *41*(April), 866–872. https://doi.org/10.1002/2013GL059010

Enderlin, E. M., & Howat, I. M. (2013). Submarine melt rate estimates for floating termini of Greenland outlet glaciers (2000 – 2010), *59*(213), 67–75. https://doi.org/10.3189/2013JoG12J049

Foga, S., Cornelis, J., Van Der Veen, C., Stearns, L. A., & Egbert, S. L. (2016). Characterization of Ice Mélange and its Implications to Terminus Stability at Helheim Glacier, Southeast Greenland.

Foga S, Stearns LA, and van der Veen CJ (2014) Application of satellite remote sensing techniques to quantify terminus and ice mélange behavior at Helheim Glacier, East Greenland. *Marine Technology Society Journal*. 48,81–91. doi: 10.4031/MTSJ.48.5.3

Frederking, R. M. W., Svec, O. J., & Imco, G. W. T. (1988). On Measuring the Shear Strength of Ice. *Appeared in Proceedings of the 9th International Symposium on Ice*, *3*(January 2010), 76–88. Retrieved from http://nparc.cisti-icist.nrc-cnrc.gc.ca/eng/view/accepted/?id=11f59b37-ce0c-425e-

a802-97e1a170daa2

Fried, M. J., Catania, G. A., Bartholomaus, T. C., Duncan, D., Davis, M., Stearns, L. A., et al. (2015). Distributed subglacial discharge drives significant submarine melt at a Greenland tidewater glacier. *Geophysical Research Letters*. https://doi.org/10.1002/2015GL065806

Fried, M. J., Catania, G. A., Stearns, L. A., Sutherland, D. A., Bartholomaus, T. C., Shroyer, E., & Nash, J. (2018). Reconciling drivers of seasonal terminus advance and retreat at thirteen central west Greenland tidewater glaciers. *Journal of Geophysical Research: Earth Surface*. https://doi.org/10.1029/2018JF004628

Gagnon, R. E., & Gammon, P. H. (1995). Triaxial experiments on iceberg and glacier ice. *Journal of Glaciology*, *41*(139), 528–540. https://doi.org/10.1017/S0022143000034869

Goldstein, R. M., & Werner, C. L. (1998). Radar interferogram filtering for geophysical applications. *Geophysical Research Letters*, *25*(21), 4035–4038. https://doi.org/10.1029/1998GL900033

Gorelick, N., Hancher, M., Dixon, M., Ilyushchenko, S., Thau, D., & Moore, R. (2017). Google Earth Engine: Planetary-scale geospatial analysis for everyone. *Remote Sensing of Environment*.

Hanna, E., Mernild, S. H., Cappelen, J., & Steffen, K. (2012). Recent warming in Greenland in a long-term instrumental (1881-2012) climatic context: I. Evaluation of surface air temperature records. *Environmental Research Letters*, *7*(4). https://doi.org/10.1088/1748-9326/7/4/045404

Holland, D., Voytenko, D., Christianson, K., Dixon, T., Mei, J., Parizek, B., et al. (2016). An Intensive Observation of Calving at Helheim Glacier, East Greenland. *Oceanography*. https://doi.org/10.5670/oceanog.2016.98

Howat, I. M., Joughin, I., Tulaczyk, S., & Gogineni, S. (2005). Rapid retreat and acceleration of Helheim Glacier, east Greenland. *Geophysical Research Letters*. https://doi.org/10.1029/2005GL024737

Howat, Ian M., Box, J. E., Ahn, Y., Herrington, A., & McFadden, E. M. (2010). Seasonal variability in the dynamics of marine-terminating outlet glaciers in Greenland. *Journal of Glaciology*, *56*(198), 601–613. https://doi.org/10.3189/002214310793146232

James, T. D., Murray, T., Selmes, N., Scharrer, K., & O'Leary, M. (2014). Buoyant flexure and basal crevassing in dynamic mass loss at Helheim Glacier. *Nature Geoscience*. https://doi.org/10.1038/ngeo2204

Joughin, I., Howat, I., Alley, R. B., Ekstrom, G., Fahnestock, M., Moon, T., et al. (2008). Ice-front variation and tidewater behavior on Helheim and Kangerdlugssuaq Glaciers, Greenland. *Journal of Geophysical Research: Earth Surface*. https://doi.org/10.1029/2007JF000837

Joughin, I., I. M. Howat, M. Fahnestock, B. Smith, W. Krabill, R. B. Alley, H. Stern, and M. Truffer (2008), Continued evolution of Jakobshavn Isbrae following its rapid speedup, J. Geophys. Res., 113, F04006, doi:10.1029/2008JF001023.

Joughin, I., Alley, R. B., & Holland, D. M. (2012). Oceanic Forcing, *Science*. (November), pg. 1172–1177.

Khan, S. A., Aschwanden, A., BjØrk, A. A., Wahr, J., Kjeldsen, K. K., & Kjær, K. H. (2015). Greenland ice sheet mass balance: A review. *Reports on Progress in Physics*, *78*(4). https://doi.org/10.1088/0034-4885/78/4/046801

Lea, J. M. (2018). Google Earth Engine Digitisation Tool (GEEDiT), and Margin change Quantification Tool (MaQiT) – simple tools for the rapid mapping and quantification of changing Earth surface.

margins., Earth Surface Dynamics

Ma, Y., & Bassis, J. N. (2019). The Effect of Submarine Melting on Calving From Marine Terminating Glaciers. *Journal of Geophysical Research: Earth Surface*, *124*(2), 334–346. https://doi.org/10.1029/2018JF004820

MacAyeal, D. R., Scambos, T. A., Hulbe, C. L., & Fahnestock, M. A. (2003). Catastrophic ice-shelf break-up by an ice-shelf-fragment-capsize mechanism. *Journal of Glaciology*, *49*(164), 22–36. https://doi.org/10.3189/172756503781830863

Medrzycka, D., Benn, D. I., Box, J. E., Copland, L., & Balog, J. (2016). Calving Behavior at Rink Isbræ, West Greenland, from Time-Lapse Photos. *Arctic, Antarctic, and Alpine Research*. https://doi.org/10.1657/AAAR0015-059

Moon, T., Joughin, I., & Smith, B. (2015). Seasonal to multiyear variability of glacier surface velocity, terminus position, and sea ice/ice mélange in northwest Greenland. *Journal of Geophysical Research: Earth Surface*. https://doi.org/10.1002/2015JF003494

Morlighem, M., Williams, C. N.,Rignot, E., An, L., Arndt, J. E.,Bamber, J. L.,… Zinglersen, K. B.(2017). BedMachine v3: Completebed topography and ocean bathymetry mapping of Greenland from multibeam echo sounding combined with mass conservation. *Geophysical Research Letters*. 44, 11,051–11,061.https://doi.org/10.1002/2017GL074954

Murray, T. (2015). Dynamics of glacier calving at the ungrounded margin of helheim glacier, southeast Greenland. *Journal of Geophysical Research: Earth Surface*, 1. https://doi.org/10.1002/2015JF003531.

Nick, F. M., Vieli, A., Howat, I. M., & Joughin, I. (2009). Large-scale changes in Greenland outlet glacier dynamics triggered at the terminus. *Nature Geoscience*, *2*(2), 110–114. https://doi.org/10.1038/ngeo394

Nye, J. F. (1957). The distribution of stress and velocity in glaciers and ice-sheets. *Proceedings of the Royal Society of London. Series A. Mathematical and Physical Sciences*, *239*(1216), 113–133. https://doi.org/10.1098/rspa.1957.0026

O'Leary, M., & Christoffersen, P. (2013). Calving on tidewater glaciers amplified by submarine frontal melting, (June). https://doi.org/10.5194/tcd-6-3287-2012

Peters, I. R., Amundson, J. M., Cassotto, R., Fahnestock, M., Darnell, K. N., Truffer, M., & Zhang, W. W. (2015). Dynamic jamming of iceberg-choked fjords, 1122–1129. https://doi.org/10.1002/2014GL062715.

Petrenko, V. F., & Whitworth, R. W. (2010). *Physics of Ice*. *Physics of Ice*. https://doi.org/10.1093/acprof:oso/9780198518945.001.0001

Petrovic, J.J. Review Mechanical properties of ice and snow. *Journal of Materials Science* **38,** 1–6 (2003). https://doi.org/10.1023/A:1021134128038

Podrasky, D., Truffer, M., Lüthi, M., & Fahnestock, M. (2014). Quantifying velocity response to ocean tides and calving near the terminus of Jakobshavn Isbræ, Greenland. *Journal of Glaciology*, *60*(222), 609–621. https://doi.org/10.3189/2014JoG13J130

Porter, C., Morin, P., Howat, I., Noh, M., Bates, B., Peterman, K. et al. (2018). ArcticDEM. *Harvard Dataverse*, 1, [Accessed: 2020]. *https://doi.org/10.7910/DVN/OHHUKH*,

Rignot, E., Velicogna, I., Van Den Broeke, M. R., Monaghan, A., & Lenaerts, J. (2011). Acceleration of

the contribution of the Greenland and Antarctic ice sheets to sea level rise. *Geophysical Research Letters*, *38*(5), 1–5. https://doi.org/10.1029/2011GL046583

Rignot, Eric, & Kanagaratnam, P. (2006). Changes in the velocity structure of the Greenland Ice Sheet. *Science*, *311*(5763), 986–990. https://doi.org/10.1126/science.1121381

Rignot, Eric, Fenty, I., Xu, Y., Cai, C., & Kemp, C. (2015). Undercutting of marine-terminating glaciers in West Greenland. *Geophysical Research Letters*. https://doi.org/10.1002/2015GL064236

Robel, A. A. (2017). Thinning sea ice weakens buttressing force of iceberg mélange and promotes calving. *Nature Publishing Group*. https://doi.org/10.1038/ncomms14596

Scambos, T., Amanda, H., Liu, C., Bohlander, J., Fastook, J., Sargent, A., et al. (2009). Ice shelf disintegration by plate bending and hydro-fracture : Satellite observations and model results of the 2008 Wilkins ice shelf break-ups. *Earth and Planetary Science Letters*, *280*(1–4), 51–60. https://doi.org/10.1016/j.epsl.2008.12.027

Schild, K. M., & Hamilton, G. S. (2013). Seasonal variations of outlet glacier terminus position in Greenland. *Journal of Glaciology*, *59*(216), 759–770. https://doi.org/10.3189/2013JoG12J238

Schulson, E. M. (1999). The structure and mechanical behavior of ice. *JOM Journal of the Minerals, Metals and Materials Society*, *51*(2), 21–27. Retrieved from http://dx.doi.org/10.1007/s11837-999-0206-4

Schulson, E. M., & Duval, P. (2009). *Creep and Fracture of Ice*. Cambridge University Press. Retrieved from http://repositorio.unan.edu.ni/2986/1/5624.pdf

Sergeant, A., Mangeney, A., Stutzmann, E., Montagner, J. P., Walter, F., Moretti, L., & Castelnau, O. (2016). Complex force history of a calving-generated glacial earthquake derived from broadband seismic inversion. *Geophysical Research Letters*, *43*(3), 1055–1065. https://doi.org/10.1002/2015GL066785

Sergeant, A., Yastrebov, V. A., Mangeney, A., Castelnau, O., Montagner, J. P., & Stutzmann, E. (2018). Numerical Modeling of Iceberg Capsizing Responsible for Glacial Earthquakes. *Journal of Geophysical Research: Earth Surface*, *123*(11), 3013–3033. https://doi.org/10.1029/2018JF004768

Sergeant, A., Mangeney, A., Yastrebov, V. A., Walter, F., Montagner, J. P., Castelnau, O., et al. (2019). Monitoring Greenland ice sheet buoyancy-driven calving discharge using glacial earthquakes. *Annals of Glaciology*, *60*(79), 75–95. https://doi.org/10.1017/aog.2019.7

Smith, L. C., Yang, K., Pitcher, L. H., Overstreet, B. T., Chu, V. W., Rennermalm, Å. K., et al. (2017). Direct measurements of meltwater runoff on the Greenland ice sheet surface. *Proceedings of the National Academy of Sciences of the United States of America*, *114*(50), E10622–E10631. https://doi.org/10.1073/pnas.1707743114

Sundal, A. V, Shepherd, A., Broeke, M. V. A. N. D. E. N., Angelen, J. V. A. N., Gourmelen, N., & Park, J. (2013). Controls on short-term variations in Greenland glacier dynamics, *59*(217), 883–892. https://doi.org/10.3189/2013JoG13J019

Sutherland, D. A., Roth, G. E., Hamilton, G. S., Mernild, S. H., Stearns, L. A., & Straneo, F. (2014). Quantifying flow regimes in a Greenland glacial fjord using iceberg drifters. *Geophysical Research Letters*, *41*(Figure 1), 8411–8420. https://doi.org/10.1002/2014GL062256.Received

Taylor, Z.J.; Gurka, R.; Kopp, G.A.; Liberzon, A.; , "Long-Duration Time-Resolved PIV to Study Unsteady Aerodynamics," Instrumentation and Measurement, IEEE Transactions on , vol.59, no.12, pp.3262-3269, Dec. 2010 doi: 10.1109/TIM.2010.2047149

Truffer M and Motyka RJ (2016) Where glaciers meet water: Subaqueous melt and its relevance to glaciers in various settings. Reviews of Geophysics 54, 220–239. doi: 10.1002/2015RG000494

Tsai, V. C., Rice, J. R., & Fahnestock, M. (2008). Possible mechanisms for glacial earthquakes. *Journal of Geophysical Research: Earth Surface*, *113*(3), 1–17. https://doi.org/10.1029/2007JF000944

Van Der Veen, C. J. (1996). Tidewater calving. *Journal of Glaciology*, *42*(141), 375–385. https://doi.org/10.3189/s0022143000004226

Vaughan, G. (1993). Relating the occurrence of crevasses to surface strain rates. *International Journal of Rock Mechanics and Mining Sciences & Geomechanics Abstracts*, *31*(3), 171. https://doi.org/10.1016/0148-9062(94)90888-5

Vieli, A., & Nick, F. M. (2011). Understanding and Modelling Rapid Dynamic Changes of Tidewater Outlet Glaciers : Issues and Implications, 437–458. https://doi.org/10.1007/s10712-011-9132-4

Voytenko, D., Dixon, T. H., Howat, I. M., Gourmelen, N., Lembke, C., Werner, C. L., et al. (2015). Multi-year observations of Breioamerkurjökull, a marine-terminating glacier in southeastern Iceland, using terrestrial radar interferometry. *Journal of Glaciology*, *61*(225), 42–54. https://doi.org/10.3189/2015JoG14J099

Voytenko, D., Stern, A., Holland, D. M., Dixon, T. H., Christianson, K., & Walker, R. T. (2015). Tidally driven ice velocity variation at Helheim Glacier , Greenland , observed with terrestrial radar interferometry, (February 2016). https://doi.org/10.3189/2015JoG14J173

Voytenko, D., Dixon, T. H., Holland, D. M., Cassotto, R., Howat, I. A. N. M., Fahnestock, M. A., et al. (2017). Acquisition of a 3 min , two-dimensional glacier velocity field with terrestrial radar interferometry, 1–8. https://doi.org/10.1017/jog.2017.28

Walter, J. I., Box, J. E., Tulaczyk, S., Brodsky, E. E., Howat, I. M., Ahn, Y., & Brown, A. (2012). Oceanic mechanical forcing of a marine-terminating Greenland glacier, *53*(60), 181–192. https://doi.org/10.3189/2012AoG60A083

Werner, C., Strozzi, T., Wiesmann, A., & Wegmüller, U. (n.d.). GAMMA ' S PORTABLE RADAR INTERFEROMETER, 1–10.

Wilson, J. T., and Horeth, J. M. (1948). Bending and shear tests on lake ice. *Transactions American Geophysical Union*. DOI:10.1029/TR029i006p00909

Xie, S., Dixon, T. H., Voytenko, D., Holland, D. M., Holland, D., & Zheng, T. (2016). Precursor motion to iceberg calving at Jakobshavn Isbræ, Greenland, observed with terrestrial radar interferometry. *Journal of Glaciology*. https://doi.org/10.1017/jog.2016.104

Zebker, H. A., & Lu, Y. (1998). Phase unwrapping algorithms for radar interferometry: residue-cut, least-squares, and synthesis algorithms. *Journal of the Optical Society of America A*, *15*(3), 586. https://doi.org/10.1364/josaa.15.000586